

Automated one-loop calculations with GOSAM

Gavin Cullen^{1,2,a}, Nicolas Greiner^{3,4,b}, Gudrun Heinrich^{3,c}, Gionata Luisoni^{5,d}, Pierpaolo Mastrolia^{3,6,e}, Giovanni Ossola^{7,8,f}, Thomas Reiter^{3,g}, Francesco Tramontano^{9,h}

¹DESY, Zeuthen, Germany

²School of Physics and Astronomy, The University of Edinburgh, Edinburgh, UK

³Max-Planck-Institut für Physik, München, Germany

⁴Department of Physics, University of Illinois at Urbana-Champaign, Urbana, USA

⁵Institute for Particle Physics Phenomenology, University of Durham, Durham, UK

⁶Dipartimento di Fisica, Università di Padova, Padova, Italy

⁷New York City College of Technology, City University of New York, New York, USA

⁸The Graduate School and University Center, City University of New York, New York, USA

⁹CERN, Geneva, Switzerland

Received: 18 January 2012 / Published online: 27 March 2012

© The Author(s) 2012. This article is published with open access at Springerlink.com

Abstract We present the program package GOSAM which is designed for the automated calculation of one-loop amplitudes for multi-particle processes in renormalisable quantum field theories. The amplitudes, which are generated in terms of Feynman diagrams, can be reduced using either D-dimensional integrand-level decomposition or tensor reduction. GOSAM can be used to calculate one-loop QCD and/or electroweak corrections to Standard Model processes and offers the flexibility to link model files for theories Beyond the Standard Model. A standard interface to programs calculating real radiation is also implemented. We demonstrate the flexibility of the program by presenting examples of processes with up to six external legs attached to the loop.

Contents

1 Introduction	2
2 Overview and algorithms	3
2.1 Overview	3
2.2 Generation and organisation of the diagrams	3
2.3 Algebraic processing	4

2.4 Code generation	7
2.5 Conventions of the amplitudes	8
3 Requirements and installation	10
3.1 Requirements	10
3.2 Download and installation	10
4 Using GOSAM	11
4.1 Setting up a simple process	11
4.2 Interfacing the code	14
4.3 Using the BLHA interface	15
4.4 Using external model files	15
5 Sample calculations and benchmarks	16
5.1 $pp \rightarrow W^- + j$ with SHERPA	16
5.2 $pp \rightarrow W^\pm + j$, EW corrections	17
5.3 $\gamma\gamma \rightarrow \gamma\gamma$	18
5.4 $pp \rightarrow \chi_1^0 \chi_1^0$ in the MSSM	18
5.5 $e^+e^- \rightarrow e^+e^- \gamma$	19
5.6 $pp \rightarrow t\bar{t}H$	20
5.7 $gg \rightarrow t\bar{t}Z$	20
5.8 $pp \rightarrow b\bar{b}b\bar{b} + X$	21
5.9 $pp \rightarrow t\bar{t}b\bar{b} + X$	21
5.10 $pp \rightarrow W^+W^-b\bar{b}$	22
5.11 $u\bar{d} \rightarrow W^+ggg$	22
5.12 $u\bar{d} \rightarrow W^+(\rightarrow \nu_e e^+)b\bar{b}$ (massive b -quark)	23
6 Conclusions	23
Acknowledgements	24
Appendix A: Examples included in the release	24
A.1 How to run the examples	25
A.2 $e^+e^- \rightarrow u\bar{u}$	25
A.3 $e^+e^- \rightarrow t\bar{t}$	25
A.4 $u\bar{u} \rightarrow d\bar{d}$	25
A.5 $gg \rightarrow gg$	26
A.6 $gg \rightarrow gZ$	26

^a e-mail: gavin.cullen@desy.de

^b e-mail: greiner@mpp.mpg.de

^c e-mail: gudrun@mpp.mpg.de

^d e-mail: Gionata.Luisoni@durham.ac.uk

^e e-mail: Pierpaolo.Mastrolia@cern.ch

^f e-mail: gossola@citytech.cuny.edu

^g e-mail: reiterth@mpp.mpg.de

^h e-mail: Francesco.Tramontano@cern.ch

A.7	$d\bar{d} \rightarrow t\bar{t}$	26
A.8	$gg \rightarrow t\bar{t}$	27
A.9	$bg \rightarrow Hb$	27
A.10	$H \rightarrow \gamma\gamma$	28
A.11	$u\bar{d} \rightarrow e^- \bar{\nu}_e$	28
A.12	$u\bar{d} \rightarrow e^- \bar{\nu}_e g$	28
A.13	$gb \rightarrow e^- \bar{\nu}_e t$	29
A.14	$\bar{u}d \rightarrow W^+ W^+ \bar{c}s$	29
Appendix B:	Explicit reduction of R_2 rational terms	30
References		30

1 Introduction

The Standard Model is currently being re-discovered at the LHC, and new exclusion limits on Beyond the Standard Model particles—and on the Higgs mass—are being delivered by the experimental collaborations with an impressive speed. Higher order corrections play an important role in obtaining bounds on the Higgs boson and New Physics. In particular, the exclusion limits for the Higgs boson would look very different if we only had leading order tools at hand. Further, it will be very important to have precise theory predictions to constrain model parameters once a signal of New Physics has been established. Therefore it is of major importance to provide tools for next-to-leading order (NLO) predictions which are largely automated, such that signal and background rates for a multitude of processes can be estimated reliably.

The need for an automation of NLO calculations has been noticed some time ago and lead to public programs like FeynArts [1] and QGraf [2] for diagram generation and FormCalc/LoopTools [3] and GRACE [4] for the automated calculation of NLO corrections, primarily in the electroweak sector. However, the calculation of one-loop amplitudes with more than four external legs were still tedious case-by-case calculations. Only very recently, conceptual and technical advances in multi-leg one-loop calculations allowed the calculation of six-point [5–24] and even seven-point [25, 26] processes at all, and opened the door to the possibility of an *automated* generation and evaluation of multi-leg one-loop amplitudes. As a consequence, already existing excellent public tools, each containing a collection of hard-coded individual processes, like e.g. MCFM [27, 28], VBFNLO [29, 30], MC@NLO [31, 32], POWHEG-Box [33, 34], POWHEL [35–37], can be flanked by flexible automated tools such that basically any process which may turn out to be important for the comparison of LHC findings to theory can be evaluated at NLO accuracy.

We have recently experienced major advances in the activity of constructing packages for fully automated one-loop calculations, see e.g. [38–43]. The concepts that lead to these advances have been recently reviewed in

[44]. Among the most important developments are the integrand-reduction technique [45, 46] and the generalized n -dimensional unitarity [47]. Their main outcome is a numerical reconstruction of a representation of the tensor structure of any one-loop integrand where the multi-particle pole configuration is manifest. As a consequence, decomposing one-loop amplitudes in terms of basic integrals becomes equivalent to reconstructing the polynomial forms of the residues to all multi-particle cuts. Within this algorithm, the integrand of a given scattering amplitude, carrying complete and explicit information on the chosen dimensional-regularisation scheme, is the only input required to accomplish the task of its evaluation. In fact, the integration is substituted by a much simpler operation, namely by polynomial fitting, which requires the sampling of the integrand on the solutions of generalised on-shell conditions.

In this article, we present the program package GOSAM which allows the automated calculation of one-loop amplitudes for multi-particle processes. Amplitudes are expressed in terms of Feynman diagrams, where the integrand is generated analytically using QGRAF [2], FORM [48], spinney [49] and haggies [50]. The individual program tasks are steered via python scripts, while the user only needs to edit an “input card” to specify the details of the process to be calculated, and launch the generation of the source code and its compilation, without having to worry about internal details of the code generation.

The program offers the option to use different reduction techniques: either the unitarity-based integrand reduction as implemented in SAMURAI [40] or traditional tensor reduction as implemented in Golem95C [51, 52] interfaced through tensorial reconstruction at the integrand level [53], or a combination of both. It can be used to calculate one-loop corrections within both QCD and electroweak theory. Beyond the Standard Model theories can be interfaced using FeynRules [54] or LanHEP [55]. The Binoth-Les Houches-interface [56] to programs providing the real radiation contributions is also included.

The advantage of generating analytic expressions for the integrand of each diagram gives the user the flexibility to organize the computation according to his own efficiency preferences. For instance, the computing algorithm can proceed either diagram-by-diagram or by grouping diagrams that share a common set of denominators (suitable for a unitarity-based reduction), and it can deal with the evaluation of the rational terms either on the same footing as the rest of the amplitude, or through an independent routine which evaluates them analytically. These options and the other features of GOSAM will be discussed in detail in the following.

In Sect. 2, after giving an overview on the diagram generation and on processing gauge-group and Lorentz algebra, we discuss the code generation and the reduction strategies.

The installation requirements are given in Sect. 3, while Sect. 4 describes the usage of GOSAM, containing all the set-up options which can be activated by editing the input card. In Sect. 5 we show results for processes of various complexity. The release of GOSAM is accompanied by the generated code for some example processes, listed in Appendix A.

2 Overview and algorithms

2.1 Overview

GOSAM produces, in a fully automated way, all the code required to perform the calculation of one-loop matrix elements. There are three main steps in the process of constructing the code: the generation of all contributing diagrams within a process directory, the generation of the `Fortran` code, and finally compiling and linking the generated code. These steps are self-contained in the sense that after each step all the files contained in the process directory could be transferred to a different machine where the next step will be carried out.

In the following sections we focus on the algorithms that are employed for the construction of the code to produce and evaluate matrix elements.

The first step (*setting up a process directory*), which consists in the generation of some general source files and the generation of the diagrams, is described in Sect. 2.2. The second step (*generating the fortran code*) is carried out by means of advanced algorithms for algebraic manipulation and code optimization which are presented in Sects. 2.3 and 2.4. The third step (*compilation and linking*) is not specific to our code generation, therefore will not be described here.

The practical procedures to be followed by the user in generating the code will be given in Sect. 4, which can be considered a short version of the user manual.

2.2 Generation and organisation of the diagrams

For the diagram generation both at tree level and one-loop level we employ the program QGRAF [2]. This program already offers several ways of excluding unwanted diagrams, for example by requesting a certain number of propagators or vertices of a certain type or by specifying topological properties such as the presence of tadpoles or on-shell propagators. Although QGRAF is a very reliable and fast generator, we extend its possibilities by adding another level of analysing and filtering over diagrams by means of `Python`. This gives several advantages: first of all, the possibilities offered by QGRAF are not always sufficient to distinguish certain classes of diagrams (see examples in Fig. 1); secondly,

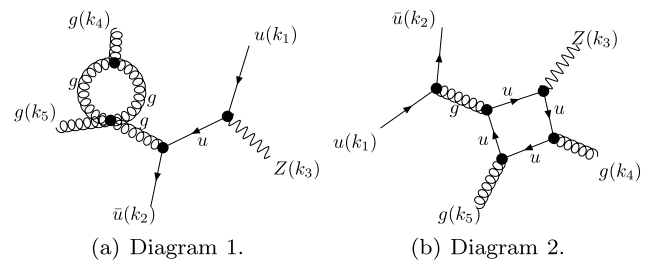


Fig. 1 Two examples for diagrams which are difficult to isolate using QGRAF. The diagram in Fig. 1(a) is zero in dimensional regularisation. However, in QGRAF there is no operator to identify this type of diagrams. In Fig. 1(b) the Z boson is emitted from a closed quark line. These diagrams form a separate gauge invariant class and could be treated separately from diagrams where the Z boson comes from an external quark line

QGRAF cannot handle the sign for diagrams with Majorana fermions in a reliable way; finally, in order to fully optimize the reduction, we want to classify and group diagrams according to the sets of their propagators.

Within our framework, QGRAF generates three sets of output files: an expression for each diagram to be processed with FORM [48], `Python` code for drawing all diagrams, and `Python` code for computing the properties of each diagram. The information about the model for QGRAF is either read from the built-in Standard Model file or is generated from a user defined LanHEP [55] or Universal FeynRules Output (UFO) [54] file.

The `Python` program automatically performs several operations:

- diagrams whose color factor turns out to be zero are dropped automatically;
- the fermion flow is determined and used to compute an overall sign for each diagram, which is relevant in the presence of Majorana fermions;
- the number of propagators containing the loop momentum, i.e. the loop size of the diagram, the tensor rank and the kinematic invariants of the associated loop integral are computed;
- diagrams with an associated vanishing loop integral (see Fig. 1(a)) are detected and flagged for the diagram selection;
- all propagators and vertices are classified for the diagram selection; diagrams containing massive quark self-energy insertions or closed massless quark loops are specially flagged.

Any one-loop diagram can be written in the form

$$\mathcal{D} = \int \frac{d^n q}{i\pi^{n/2}} \frac{\mathcal{N}(q)}{\prod_{l=1}^N [(q + r_l)^2 - m_l^2 + i\delta]}, \quad (1)$$

where the numerator is a polynomial of tensor¹ rank r .

$$\mathcal{N}(q) = C_0 + C_1^{\mu_1} q_{\mu_1} + \cdots + C_r^{\mu_1 \dots \mu_r} q_{\mu_1} \cdots q_{\mu_r}, \quad (2)$$

and the $N \times N$ kinematic matrix is defined as

$$S_{ij} = (r_i - r_j)^2 - m_i^2 - m_j^2. \quad (3)$$

All masses can be either real or complex. Important information about the integrals that will appear in the reduction of each one-loop diagram is contained in the tensor rank r of the loop integral and its kinematic matrix S_{ij} .

We define a preorder relation on one-loop diagrams, such that $\mathcal{D}_1 \preceq \mathcal{D}_2$ if their associated matrices $S(\mathcal{D}_1)$ and $S(\mathcal{D}_2)$ are related by a finite (not necessarily unique) chain of transformations

$$S(\mathcal{D}_2) \xrightarrow{T_1} S' \xrightarrow{T_2} \cdots \xrightarrow{T_m} S(\mathcal{D}_1), \quad (4)$$

where each transformation is one of the following:

- the identity,
- the simultaneous permutation of rows and columns,
- the simultaneous deletion of the row and column with the same index, which corresponds to *pinching* the corresponding propagator in the diagram.

The relation “ \preceq ” can be read as “appears in the reduction of”. Our algorithm groups the one-loop diagrams $\mathcal{D}_1, \dots, \mathcal{D}_D$ of a process into subsets V_1, \dots, V_G such that

- V_1, \dots, V_G form a partition of $\{\mathcal{D}_1, \dots, \mathcal{D}_D\}$ and
- each cell V_i contains a maximum element $\max V_i \in V_i$, such that $\mathcal{D} \preceq \max V_i, \forall \mathcal{D} \in V_i$.

The partitioning procedure provides an important gain in efficiency, because while carrying out the tensor reduction for the diagram $\max V_i$, all other diagrams in the same cell V_i are reduced with virtually no additional computational cost. The gain in efficiency can be observed when reducing the diagram using the OPP method [45] and its implementations in CutTools [57] and SAMURAI [40], as well as in classical tensor reduction methods as implemented e.g. in Go1em95C [51, 52], PJFry [58] and LoopTools [3, 59].

In order to draw the diagrams, we first compute an ordering of the external legs which allows for a planar embedding of the graph. Such ordering can always be found for a tree or a one-loop graph since non-planar graphs only start to appear in diagrams with two or more loops. After the legs have been assigned to the vertices of a regular polygon, we use our own implementation of the algorithms described in [60] for fixing the coordinates of the remaining vertices; the algorithm has been extended to determine an appealing layout also for graphs containing tadpoles. Starting from these

coordinates and using the package Axodraw [61], GOSAM generates a L^AT_EX file that contains graphical representations of all diagrams.

2.3 Algebraic processing

2.3.1 Color algebra

In the models used by GOSAM, we allow one unbroken gauge group $SU(N_C)$ to be treated implicitly; any additional gauge group, broken or unbroken, needs to be expanded explicitly. Any particle of the model may be charged under the $SU(N_C)$ group in the trivial, (anti-)fundamental or adjoint representation. Other representations are currently not implemented.

For a given process we project each Feynman diagram onto a color basis consisting of strings of generators $T_{ii_1}^{A_1} T_{i_1 i_2}^{A_2} \cdots T_{i_{p-1} j}^{A_p}$ and Kronecker deltas δ_{ij} but no contractions of adjoint indices and no structure constants f^{ABC} . Considering, for example, the process

$$u(1) + \bar{u}(2) \rightarrow Z(3) + g(4) + g(5)$$

GOSAM finds the color basis

$$\begin{aligned} |c_1\rangle &= q_{i_1}^{(1)} \bar{q}_{j_2}^{(2)} g_{(4)}^{A_4} g_{(5)}^{A_5} (T^{A_4} T^{A_5})_{j_2 i_1}, \\ |c_2\rangle &= q_{i_1}^{(1)} \bar{q}_{j_2}^{(2)} g_{(4)}^{A_4} g_{(5)}^{A_5} (T^{A_5} T^{A_4})_{j_2 i_1}, \\ |c_3\rangle &= q_{i_1}^{(1)} \bar{q}_{j_2}^{(2)} g_{(4)}^{A_4} g_{(5)}^{A_5} \delta_{j_2 i_1} \text{tr}\{T^{A_5} T^{A_4}\}, \end{aligned}$$

where $q_i^{(\bullet)}$ and $g_{(\bullet)}^{A_\bullet}$ are the color parts of the quark and gluon wave functions respectively. The dimension of this color basis for N_g external gluons and $N_{q\bar{q}}$ quark-antiquark pairs is given by [62]:

$$d(N_g, N_{q\bar{q}}) = \sum_{i=0}^{N_g} (-1)^i \binom{N_g}{i} \cdot (N_g + N_{q\bar{q}} - i)!. \quad (5)$$

It should be noted that the color basis constructed in this way is not a basis in the mathematical sense, as one can find linear relations between the vectors $|c_i\rangle$ once the number of external partons is large enough.

Any Feynman diagram can be reduced to the form

$$\mathcal{D} = \sum_{i=1}^k \mathcal{C}_i |c_i\rangle \quad (6)$$

for the process specific color basis $|c_1\rangle, \dots, |c_k\rangle$ by applying the following set of relations:

$$T_{ij}^A T_{kl}^A = T_R \left(\delta_{il} \delta_{kj} - \frac{1}{N_C} \delta_{ij} \delta_{kl} \right), \quad (7)$$

$$f^{ABC} = \frac{1}{i T_R} (T_{ij}^A T_{jk}^B T_{ki}^C - T_{ij}^A T_{jk}^C T_{ki}^B). \quad (8)$$

¹ Index contractions in (2) are understood in n -dimensional space.

The same set of simplifications is used to compute the matrices $\langle c_i | c_j \rangle$ and $\langle c_i | T_I \cdot T_J | c_j \rangle$. The former is needed for squaring the matrix element, whereas the latter is used to provide color correlated Born matrix elements which we use for checking the IR poles of the virtual amplitude and also to provide the relevant information for parton showers like POWHEG [33, 34, 63]. For the above example, GOSAM obtains²

$$\langle c_i | c_j \rangle = T_R C_F \begin{pmatrix} (N_C^2 - 1) & -1 & N_C \\ -1 & (N_C^2 - 1) & N_C \\ N_C & N_C & N_C^2 \end{pmatrix}. \quad (9)$$

Similarly, the program computes the matrices $\langle c_i | T_I \cdot T_J | c_j \rangle$ for all pairs of partons I and J .

If $\mathcal{M}^{(0)}$ denotes the tree-level matrix element of the process and we have

$$\mathcal{M}^{(0)} = \sum_{j=1}^k \mathcal{C}_j^{(0)} |c_j\rangle, \quad (10)$$

then the square of the tree level amplitude can be written as

$$|\mathcal{M}^{(0)}|^2 = \sum_{i,j=1}^k (\mathcal{C}_i^{(0)})^* \mathcal{C}_j^{(0)} \langle c_i | c_j \rangle. \quad (11)$$

For the interference term between leading and next-to-leading order we use a slightly different philosophy. First of all we note that it is sufficient to focus on a single group V_α as defined in Sect. 2.2,

$$\begin{aligned} & (\mathcal{M}^{(1)})^\dagger \mathcal{M}^{(0)} + h.c. \\ &= \sum_\alpha \int \frac{d^n q}{i\pi^{n/2}} \frac{\mathcal{N}_\alpha(q)}{\prod_{l=1}^N [(q+r_l)^2 - m_l^2 + i\delta]} + h.c. \end{aligned} \quad (12)$$

In order to reduce the complexity at the level of the reduction, we perform the contraction with the tree-level already at the integrand level,

$$\mathcal{N}_\alpha(q) = \sum_{i,j=1}^k \langle c_i | c_j \rangle (\mathcal{C}_i^{(0)})^* \mathcal{C}_j^{(1)}(q), \quad (13)$$

where $\mathcal{C}_j^{(1)}$ is formed by the sum over the corresponding coefficients of all diagrams $\mathcal{D} \in V_\alpha$.

2.3.2 Lorentz algebra

In this section we discuss the algorithms used by GOSAM to transform the coefficients $\mathcal{C}_i^{(0)}$ and $\mathcal{C}_i^{(1)}(q)$, as defined in the previous section, such that the result is suitable for efficient numerical evaluation. One of the major goals is to split

the n -dimensional algebra ($n = 4 - 2\varepsilon$) into strictly four-dimensional objects and symbols representing the higher-dimensional remainder.

In GOSAM we have implemented the 't Hooft-Veltman scheme (HV) and dimensional reduction (DRED). In both schemes all external vectors (momenta and polarisation vectors) are kept in four dimensions. Internal vectors, however, are kept in the n -dimensional vector space. We adopt the conventions used in [49], where \hat{k} denotes the four-dimensional projection of an in general n -dimensional vector k . The $(n-4)$ -dimensional orthogonal projection is denoted as \tilde{k} . For the integration momentum q we introduce in addition the symbol $\mu^2 = -\tilde{q}^2$, such that

$$q^2 = \hat{q}^2 + \tilde{q}^2 = \hat{q}^2 - \mu^2. \quad (14)$$

We also introduce suitable projectors by splitting the metric tensor

$$\begin{aligned} g^{\mu\nu} &= \hat{g}^{\mu\nu} + \tilde{g}^{\mu\nu}, & \hat{g}^{\mu\nu} \tilde{g}_{\nu\rho} &= 0, \\ \hat{g}_\mu^\mu &= 4, & \tilde{g}_\mu^\mu &= n-4. \end{aligned} \quad (15)$$

In the following, we describe the 't Hooft algebra in detail. For DRED, the only differences are that the numerator algebra is performed in four dimensions for both external and internal vectors (i.e. $q \equiv \hat{q}$) and that in the very end all appearances of q^2 are replaced by $\hat{q}^2 - \mu^2$.

Wave functions and propagators GOSAM contains a library of representations of wave functions and propagators up to spin two.³ The exact form of the interaction vertices is taken from the model files.

The representation of all wave functions with non-trivial spin is based on massless spinors. Each massive external vector p_i is replaced by its light-cone projection l_i with respect to a lightlike reference vector k ,

$$p_i^\mu = l_i^\mu + \frac{p_i^2}{2p_i \cdot k} k^\mu. \quad (16)$$

For spin $1/2$ particles we use the assignment of wave functions as shown in Table 1; here, we quote the definition of the massive spinors from [49] assuming the splitting of (16):

$$|p^\pm\rangle = |l\rangle \pm \frac{\sqrt{p^2}}{[lk]} |k], \quad |p^\pm] = |l\rangle \pm \frac{\sqrt{p^2}}{\langle lk\rangle} |k\rangle, \quad (17a)$$

$$\langle p^\pm| = \langle l| \pm \frac{\sqrt{p^2}}{[kl]} [k|, \quad [p^\pm| = [l| \pm \frac{\sqrt{p^2}}{\langle kl\rangle} \langle k|. \quad (17b)$$

²In the actual code the results are given in terms of T_R and N_C only.

³Processes with particles of spin $3/2$ and spin 2 have not been tested extensively. Furthermore, these processes can lead to integrals where the rank is higher than the loop size, which at the moment are neither implemented in SAMURAI nor in Go1em95C.

Table 1 Assignment of quark and lepton wave functions. We label the physical spin states by $j_3 = \pm 1$, which is twice the 3-component of the spin. The wave functions assigned in Table (a) are mapped onto the bracket notation used in `spinney` [49] as defined in Tables (b) and (c)

(a) Assignment of initial and final states for quarks and leptons			(b) Wave functions for massless fermions		(c) Wave functions for massive fermions	
	l^-, q	l^+, \bar{q}				
initial	$u_\alpha(k, j_3)$	$\bar{v}_\alpha(k, j_3)$	$u_\alpha(k, +1) = v_\alpha(k, -1) = k\rangle$		$u_\alpha(p, +1) = p^+\rangle$	$\bar{u}_\alpha(p, +1) = [p^+ $
			$u_\alpha(k, -1) = v_\alpha(k, +1) = k\rangle$		$u_\alpha(p, -1) = p^+\rangle$	$\bar{u}_\alpha(p, -1) = [p^+ $
final	$\bar{u}_\alpha(k, j_3)$	$v_\alpha(k, j_3)$	$\bar{u}_\alpha(k, +1) = \bar{v}_\alpha(k, -1) = [k $		$v_\alpha(p, +1) = p^-\rangle$	$\bar{v}_\alpha(p, +1) = \langle p^- $
			$\bar{u}_\alpha(k, -1) = \bar{v}_\alpha(k, +1) = [k $		$v_\alpha(p, -1) = p^-\rangle$	$\bar{v}_\alpha(p, -1) = \langle p^- $

In order to preserve the condition that for any loop integral the tensor rank does not exceed the number of loop propagators we fix all gauge boson propagators to be in Feynman gauge. Their wave functions are constructed as [64]

$$\varepsilon_\mu(p, +1) = \frac{\langle q | \gamma_\mu | p^b \rangle}{\sqrt{2} \langle q p^b \rangle}, \quad \varepsilon_\mu(p, -1) = \frac{[q | \gamma_\mu | p^b \rangle}{\sqrt{2} [p^b q]}, \quad (18)$$

where $p^b = p$ in the massless case and $p^b = l$ according to (16) in the massive case. In the latter case the third polarisation is defined as

$$\varepsilon_\mu(p, 0) = \frac{1}{\sqrt{p^2}} (2p_\mu^b - p_\mu). \quad (19)$$

The wave functions and propagators for spin $3/2$ and spin 2 particles correspond to those in [65].

Simplifications Once all wave functions and propagators have been substituted by the above definitions and all vertices have been replaced by their corresponding expressions from the model file then all vector-like quantities and all metric tensors are split into their four-dimensional and their orthogonal part. As we use the 't Hooft algebra, γ_5 is defined as a purely four-dimensional object, $\gamma_5 = i \epsilon_{\mu\nu\rho\sigma} \hat{\gamma}^\mu \hat{\gamma}^\nu \hat{\gamma}^\rho \hat{\gamma}^\sigma$. By applying the usual anti-commutation relations for Dirac matrices we can always separate the four-dimensional and $(n-4)$ -dimensional parts of Dirac traces, as we can use the fact that [49, 62]

$$\begin{aligned} \text{tr}(1) \cdot \text{tr}(\hat{\gamma}_{\mu_1} \cdots \hat{\gamma}_{\mu_l} \tilde{\gamma}_{\mu_{l+1}} \cdots \tilde{\gamma}_{\mu_{l+p}}) \\ = \text{tr}(\hat{\gamma}_{\mu_1} \cdots \hat{\gamma}_{\mu_l}) \cdot \text{tr}(\tilde{\gamma}_{\mu_{l+1}} \cdots \tilde{\gamma}_{\mu_{l+p}}). \end{aligned} \quad (20)$$

The same logic applies to open spinor lines such as [49]

$$\begin{aligned} \text{tr}(1) \cdot \langle k_1 | \hat{\gamma}_{\mu_1} \cdots \hat{\gamma}_{\mu_l} \tilde{\gamma}_{\mu_{l+1}} \cdots \tilde{\gamma}_{\mu_{l+p}} | k_2 \rangle \\ = \langle k_1 | \hat{\gamma}_{\mu_1} \cdots \hat{\gamma}_{\mu_l} | k_2 \rangle \cdot \text{tr}(\tilde{\gamma}_{\mu_{l+1}} \cdots \tilde{\gamma}_{\mu_{l+p}}). \end{aligned} \quad (21)$$

While the $(n-4)$ -dimensional traces are reduced completely to products of $(n-4)$ -dimensional metric tensors $\tilde{g}^{\mu\nu}$, the four-dimensional part is treated such that the number of terms in the resulting expression is kept as small

as possible. Any spinor line or trace is broken up at any position where a light-like vector appears. Furthermore, Chisholm identities are used to resolve Lorentz contractions between both Dirac traces and open spinor lines. If any traces remain we use the built-in trace algorithm of FORM [48].

In the final result we can always avoid the explicit appearance of Levi-Civita tensors, noticing that any such tensor is contracted with at least one light-like vector⁴ \hat{k}^μ , and we can replace

$$\hat{k}^\mu \epsilon_{\mu\nu\rho\sigma} = -\frac{i}{4} ([k | \hat{\gamma}_\nu \hat{\gamma}_\rho \hat{\gamma}_\sigma | k] - [k | \hat{\gamma}_\nu \hat{\gamma}_\rho \hat{\gamma}_\sigma | k]). \quad (22)$$

Hence, the kinematic part of the numerator, at the end of our simplification algorithm, is expressed entirely in terms of:

- spinor products of the form $\langle k_i k_j \rangle$, $[k_i k_j]$ or $[k_i | \hat{\gamma}^\mu | k_j] \cdot \hat{q}_\mu$,
- dot products $\hat{k}_i \cdot \hat{k}_j$ or $\hat{k}_i \cdot \hat{q}$,
- constants of the Lagrangian such as masses, widths and coupling constants,
- the symbols $\mu^2 = \hat{q}^2 - q^2$ and $\varepsilon = (n-4)/2$.

Treatment of R_2 rational terms In our representation for the numerator of one-loop diagrams, terms containing the symbols μ^2 or ε can lead to a so-called R_2 term [66], which contributes to the rational part of the amplitude. In general, there are two ways of splitting the numerator function:

$$\begin{aligned} \mathcal{N}(\hat{q}, \mu^2, \varepsilon) = \mathcal{N}_0(\hat{q}, \mu^2) + \varepsilon \mathcal{N}_1(\hat{q}, \mu^2) \\ + \varepsilon^2 \mathcal{N}_2(\hat{q}, \mu^2) \end{aligned} \quad (23a)$$

or, alternatively,

$$\mathcal{N}(\hat{q}, \mu^2, \varepsilon) = \hat{\mathcal{N}}(\hat{q}) + \tilde{\mathcal{N}}(\hat{q}, \mu^2, \varepsilon). \quad (23b)$$

It should be noted that in (23a) the terms \mathcal{N}_1 and \mathcal{N}_2 do not arise in DRED, where only terms containing μ^2 contribute to R_2 . Instead of relying on the construction of R_2

⁴Any external massive vector at this point has been replaced by a pair of light-like ones. Contractions between two Levi-Civita symbols can be resolved to products of metric tensors.

from specialized Feynman rules [67–70], we generate the R_2 part along with all other contributions without the need to separate the different parts. For efficiency reasons, however, we provide an *implicit* and an *explicit* construction of the R_2 terms.

The implicit construction uses the splitting of (23a) and treats all three numerator functions \mathcal{N}_i on equal grounds. Each of the three terms is reduced separately in a numerical reduction and the Laurent series of the three results are added up taking into account the powers of ε .

The explicit construction of R_2 is based on the assumption that each term in $\tilde{\mathcal{N}}$ in (23b) contains at least one power of μ^2 or ε . The expressions for those integrals are relatively simple and known explicitly. Hence, the part of the amplitude which originates from $\tilde{\mathcal{N}}$ is computed analytically whereas the purely four-dimensional part $\hat{\mathcal{N}}$ is passed to the numerical reduction.

2.4 Code generation

2.4.1 Abbreviation system

To prepare the numerator functions of the one-loop diagrams for their numerical evaluation, we separate the symbol μ^2 and dot products involving the momentum \hat{q} from all other factors. All subexpressions which do not depend on either \hat{q} or μ^2 are substituted by abbreviation symbols, which are evaluated only once per phase space point. Each of the two parts is then processed using haggies [50], which generates optimized Fortran code for their numerical evaluation. For each diagram we generate an interface to SAMURAI [40], Golem95C [52] and/or PJFRY [58]. The two latter codes are interfaced using tensorial reconstruction at the integrand level [53].

2.4.2 Reduction strategies

In the implementation of GOSAM, great emphasis has been put on maintaining flexibility with respect to the reduction algorithm that the user decides to use. On the one hand, this is important because the best choice of the reduction method in terms of speed and numerical stability can strongly depend on the specific process. On the other hand, we tried to keep the code flexible to allow further extensions to new reduction libraries, such that GOSAM can be used as a laboratory for interfacing future methods with a realistic environment.

Our standard choice for the reduction is SAMURAI, which provides a very fast and stable reduction in a large part of the phase space. Furthermore, SAMURAI reports to the client code if the quality of the reconstruction of the numerator suffices the numerical requirements (for details we refer to [40]). In GOSAM we use this information to

trigger an alternative reduction with either Golem95C [52] or PJFRY [58] whenever these reconstruction tests fail, as shown in Fig. 2. The reduction algorithms implemented in these libraries extend to phase space regions of small Gram determinants and therefore cover most cases in which on-shell methods cannot operate sufficiently well. This combination of on-shell techniques and traditional tensor reduction is achieved using tensorial reconstruction at the integrand level [53], which also provides the possibility of running on-shell methods with a reconstructed numerator. In addition to solving the problem of numerical instabilities, in some cases this option can reduce the computational cost of the reduction. Since the reconstructed numerator is typically of a form where kinematics and loop momentum dependence are already separated, the use of a reconstructed numerator tends to be faster than the original procedure, in particular in cases with a large number of legs and low rank.

The flowchart in Fig. 2 summarizes all possible reduction strategies which are currently implemented. The strategy in use is selected by assigning the variable `reduction_interoperation` in the generated Fortran code. The availability of the branches is determined during code generation by activating (at least one of) the extensions (`samurai`, `golem95`, `pj fry`) in the input card.

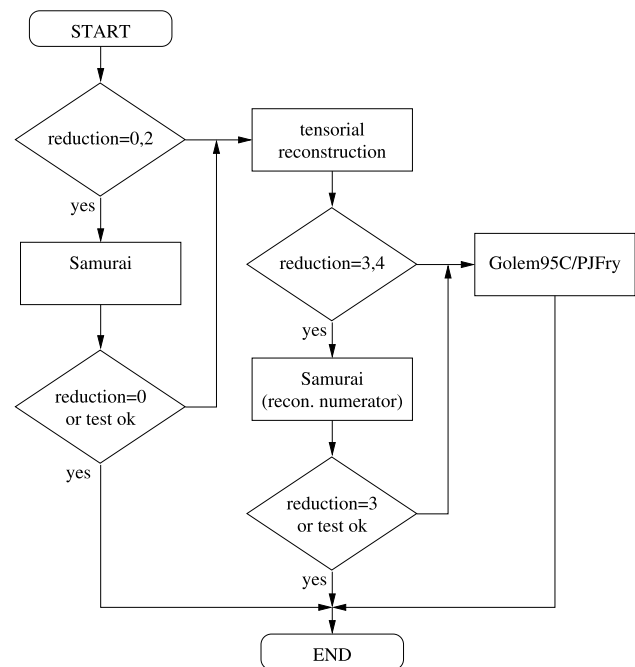


Fig. 2 Reduction strategies currently implemented in GOSAM: the reduction algorithm is chosen by setting the variable `reduction_interoperation` in the generated Fortran code and can be modified at run time. 0: SAMURAI only; 1: Golem95C only; 2: SAMURAI with rescue option (Golem95C); 3: SAMURAI with numerator from tensorial reconstruction; 4: same as 3 but with rescue option (Golem95C). 11, 12 and 14 are the same as 1, 2, 3 (respectively) with the difference that PJFRY is used instead of Golem95C.

Switching between active branches is possible at run time. In detail, the possible choices for the variable `reduction_interoperation` are the following:

- 0 the numerators of the one-loop diagrams are reduced by SAMURAI, no rescue system is used in case the reconstruction test fails;
- 1 the tensor coefficients of the numerators are reconstructed using the *tensorial reconstruction at the integrand level*, the numerator is expressed in terms of tensor integral form factors which are evaluated using Golem95C;
- 2 the numerators are reduced by SAMURAI; whenever the reconstruction test fails, numerators are reduced using the option 1 as a backup method;
- 3 tensorial reconstruction is used to compute the tensor coefficients; SAMURAI is employed for the reduction of the reconstructed numerator, no rescue system is used;
- 4 as in option 3, SAMURAI is used to reduce the reconstructed numerator, Golem95C is used as backup option;
- 11 same as 1 but PJFry is used instead of Golem95C;
- 12 same as 2 but PJFry is used instead of Golem95C;
- 14 same as 4 but PJFry is used instead of Golem95C.

It is difficult to make a statement about the “optimal” reduction method because this depends on the process under consideration. For multi-leg processes, e.g. $b\bar{b}b\bar{b}$ production, we found that SAMURAI is clearly superior to tensor reduction in what concerns timings and size of the code. Concerning points which need a special treatment, we did not make extensive studies using traditional tensor reduction only, but one can certainly say that the combination of SAMURAI and tensorial reconstruction seems to be optimal in what concerns the avoidance of numerical instabilities due to inverse Gram determinants.

2.5 Conventions of the amplitudes

In this section we briefly discuss the conventions chosen for the results returned by GOSAM. Depending on the actual setup for a given process, in particular if an imported model file is used, conventions may be slightly different. Here we restrict the discussion to the case where the user wants to compute QCD corrections to a process and in the setup files he has put $g_s = 1$. In this case, the tree-level matrix element squared can be written as

$$|\mathcal{M}|_{\text{tree}}^2 = \mathcal{A}_0^\dagger \mathcal{A}_0 = (g_s)^{2b} \cdot a_0. \quad (24)$$

The fully renormalised matrix element at one-loop level, i.e. the interference term between tree-level and one-loop, can

be written as

$$\begin{aligned} |\mathcal{M}|_{1\text{-loop}}^2 &= \mathcal{A}_1^\dagger \mathcal{A}_0 + \mathcal{A}_0^\dagger \mathcal{A}_1 = 2 \cdot \Re(\mathcal{A}_0^\dagger \mathcal{A}_1) \\ &= |\mathcal{M}|_{\text{bare}}^2 + |\mathcal{M}|_{\text{ct}, \delta m_Q}^2 + |\mathcal{M}|_{\text{ct}, \alpha_s}^2 + |\mathcal{M}|_{\text{wf}, g}^2 + |\mathcal{M}|_{\text{wf}, Q}^2 \\ &= \frac{\alpha_s(\mu)}{2\pi} \frac{(4\pi)^\varepsilon}{\Gamma(1-\varepsilon)} \cdot (g_s)^{2b} \cdot \left[c_0 + \frac{c_{-1}}{\varepsilon} + \frac{c_{-2}}{\varepsilon^2} + \mathcal{O}(\varepsilon) \right]. \end{aligned} \quad (25)$$

A call to the subroutine `amplitude` returns an array consisting of the four numbers $(a_0, c_0, c_{-1}, c_{-2})$ in this order. The average over initial state colours and helicities is included in the default setup. In cases where the process is loop induced, i.e. the tree level amplitude is absent, the program returns the values for $\mathcal{A}_1^\dagger \mathcal{A}_1$ where a factor

$$\left(\frac{\alpha_s(\mu)}{2\pi} \frac{(4\pi)^\varepsilon}{\Gamma(1-\varepsilon)} \right)^2$$

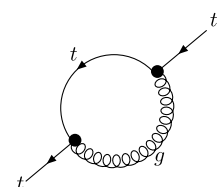
has been pulled out.

After all UV-renormalisation contributions have been taken into account correctly, only IR-singularities remain, which can be computed using the routine `ir_subtractions`. This routine returns a vector of length two, containing the coefficients of the single and the double pole, which should be equal to (c_{-1}, c_{-2}) and therefore can be used as a check of the result.

Ultraviolet renormalisation in QCD For UV-renormalisation we use the $\overline{\text{MS}}$ scheme for the gluon and all massless quarks, whereas a subtraction at zero momentum is chosen for massive quarks [71]. Currently, counterterms are only provided for QCD corrections. In the case of electroweak corrections only unrenormalised results can be produced automatically.

For computations involving loop propagators for massive fermions, we introduced the automatic generation of a mass counter term needed for the on-shell renormalisation of the massive particle. Here, we exploit the fact that such a counter term is strictly related to the massive fermion self energy bubble diagrams (see Fig. 3). As described in Sect. 2.2, the program GOSAM analyzes all generated diagrams. In that step also self-energy insertions of massive

Fig. 3 Feynman diagram of a massive quark self energy in QCD. For this type of diagram GOSAM automatically generates UV-counterterms



quarks are detected, where we make the replacement

$$\begin{aligned} & \frac{(q + r + m) \cdot g^{\mu\nu}}{[(q + r)^2 - m^2]q^2} \\ & \rightarrow \frac{(q + r + m) \cdot g^{\mu\nu}}{[(q + r)^2 - m^2]q^2} + \frac{m}{4} \left[\frac{6q \cdot r + 3(r^2 - m^2)}{m^2} \right. \\ & \quad \left. + \frac{3(4 + 1_{\text{HV}})\mu^2}{r^2 - 3m^2} \right] \frac{g^{\mu\nu}}{[(q + r)^2 - m^2]q^2}. \end{aligned} \quad (26)$$

The symbol 1_{HV} is one in the 't Hooft Veltman scheme and zero in DRED.

Performing the integral, contracting the expression with the QCD vertices at both sides and multiplying the missing factor of $(2\pi)^{-1}$ we retrieve the expression for the mass counter-term,

$$\frac{\delta m}{m} = \frac{\alpha_s}{2\pi} \frac{(4\pi)^\varepsilon}{\Gamma(1-\varepsilon)} \frac{C_F}{2} \left(\frac{\mu^2}{m^2} \right)^\varepsilon \left[\frac{3}{\varepsilon} + 5 - 1_{\text{HV}} \right]. \quad (27)$$

Furthermore, the renormalisation of α_s leads to a term of the form

$$\begin{aligned} |\mathcal{M}|_{\text{ct},\alpha_s}^2 = & b \cdot \frac{\alpha_s}{2\pi} \frac{(4\pi)^\varepsilon}{\Gamma(1-\varepsilon)} |\mathcal{M}|_{\text{tree}}^2 \cdot \left[-\frac{\beta_0}{\varepsilon} \right. \\ & \left. + \frac{2T_R}{3\varepsilon} \sum_{q=N_f+1}^{N_f+N_{f,h}} \left(\frac{\mu^2}{m_q^2} \right)^\varepsilon + \frac{C_A}{6}(1 - 1_{\text{HV}}) \right], \end{aligned} \quad (28)$$

with $\beta_0 = (11C_A - 4T_R N_f)/6$, N_f being the number of light quark flavours, $N_{f,h}$ the number of heavy flavours, and b is the power of the coupling in the Born amplitude as defined in (24). The last term of (28) provides the finite renormalisation needed to compensate the scheme dependence of α_s ,

$$\alpha_s^{\text{DR}} = \alpha_s^{\overline{\text{MS}}} \left(1 + \frac{C_A}{6} \frac{\alpha_s^{\overline{\text{MS}}}}{2\pi} \right). \quad (29)$$

A further contribution consists of the wave-function renormalisation of massive external quark lines. If we denote the set of external massive quark lines by $\mathcal{Q}_h = \{Q_1(m_1), \dots, Q_p(m_p)\}$ we obtain

$$\begin{aligned} |\mathcal{M}|_{\text{wf},Q}^2 = & -\frac{\alpha_s}{2\pi} \frac{(4\pi)^\varepsilon}{\Gamma(1-\varepsilon)} \frac{C_F}{2} \\ & \times \sum_{Q(m) \in \mathcal{Q}_h} \left(\frac{\mu^2}{m^2} \right)^\varepsilon \left[\frac{3}{\varepsilon} + 5 - 1_{\text{HV}} \right] \cdot |\mathcal{M}|_{\text{tree}}^2. \end{aligned} \quad (30)$$

Finally, also the wave function of the gluon receives a contribution from the presence of heavy quarks in closed fermion

loops. If N_g is the number of external gluon lines, this contribution can be written as

$$\begin{aligned} |\mathcal{M}|_{\text{wf},g}^2 = & -\frac{\alpha_s}{2\pi} \frac{(4\pi)^\varepsilon}{\Gamma(1-\varepsilon)} N_g \frac{2T_R}{3\varepsilon} \\ & \times \sum_{q=N_f+1}^{N_f+N_{f,h}} \left(\frac{\mu^2}{m_q^2} \right)^\varepsilon \cdot |\mathcal{M}|_{\text{tree}}^2. \end{aligned} \quad (31)$$

At the level of the generated Fortran code the presence of these contributions can be controlled by a set of variables defined in the module `config.f90`. The variable `renormalisation` can be set to 0, 1, or 2. If `renormalisation=0`, none of the counterterms are present. If `renormalisation=2` only $|\mathcal{M}|_{\text{ct},\delta m_Q}^2$ is included, which is the counterterm stemming from all terms of the type of (27) contributing to the amplitude.

In the case where `renormalisation=1` a more fine-grained control over the counterterms is possible.

`renorm_logs`: if set to *false*, in all counterterms the generation of logarithms is disabled, i.e. factors of the form $(\bullet)^\varepsilon$ in (27) to (31) are replaced by one.

`renorm_beta`: if set to *false*, the counterterm $|\mathcal{M}|_{\text{ct},\alpha_s}^2$ is set to zero.

`renorm_mqwf`: if set to *false*, the counterterm $|\mathcal{M}|_{\text{wf},Q}^2$ is set to zero.

`renorm_mqse`: if set to *false*, the counterterm $|\mathcal{M}|_{\text{ct},\delta m_Q}^2$ is set to zero.

`renorm_decoupling` if set to *false*, the counterterm $|\mathcal{M}|_{\text{wf},g}^2$ is set to zero.

The default settings for `renormalisation=1` are *true* for all the `renorm` options listed above.

Finite renormalisation of γ_5 in QCD In the 't Hooft Veltman scheme, a finite renormalisation term for γ_5 is required beyond tree level. The relevant terms are generated only if `fr5` is added in the input card to the list of extensions before code generation. Currently, the automatic generation of this finite contribution is not performed if model files different from the built-in model files are used. In agreement with [72] and [73] we replace the axial component at each vertex,

$$\gamma^\mu \gamma_5 \rightarrow \frac{1}{2} Z_{\text{axial}} (\gamma^\mu \gamma_5 - \gamma_5 \gamma^\mu), \quad (32)$$

with

$$Z_{\text{axial}} = 1 - 2 \frac{\alpha_s}{2\pi} C_F \cdot 1_{\text{HV}}. \quad (33)$$

Once it is generated, this contribution can be switched on and off at run-time through the variable `renorm_gamma5`, which is defined in the module `config.f90`.

Conversion between the schemes In GOSAM we have implemented two different schemes, the 'tHooft Veltman scheme and dimensional reduction. By default, the former is used, while the latter can be activated by adding the extension `dred`. If a QCD computation has been done in dimensional reduction the result can be converted back to the 'tHooft Veltman scheme by adding a contribution for each external massless parton,

$$|\mathcal{M}^{\text{CDR}}|_{1\text{-loop}}^2 = |\mathcal{M}^{\text{DR}}|_{1\text{-loop}}^2 - \frac{\alpha_s}{2\pi} |\mathcal{M}^{\text{DR}}|_{\text{tree}}^2 \sum_{I=1}^{N_{\text{ext}}} \tilde{\gamma}_I^{\text{DR}}, \quad (34)$$

with $\tilde{\gamma}_q^{\text{DR}} = \tilde{\gamma}_q^{\text{DR}} = C_F/2$ and $\tilde{\gamma}_g^{\text{DR}} = C_A/6$. This conversion can be switched on by setting `convert_to_cdr` to `true` in the module `config.f90`. At one-loop level, the 'tHooft Veltman scheme and conventional dimensional regularisation (CDR) are equivalent in the sense that $\tilde{\gamma}_I^{\text{thv}} = 0$ for all partons.

3 Requirements and installation

3.1 Requirements

The program GOSAM is designed to run in any modern Linux/Unix environment; we expect that Python (≥ 2.6), Java (≥ 1.5) and Make are installed on the system. Furthermore, a Fortran 95 compiler is required in order to compile the generated code. Some Fortran 2003 features are used if one wants to make use of the Les Houches interface [56]. We have tried all examples using gfortran versions 4.1 and 4.5.

On top of a standard Linux environment, the programs FORM [48], version ≥ 3.3 (newer than Aug. 11, 2010) and QGRAF [2] need to be installed on the system. Whereas spinney [49] and haggies [50] are part of GOSAM and are not required to be installed separately, at least one of the libraries SAMURAI [40] and Golem95C [52] needs to be present at compile time of the generated code. Optionally, PJFRY [58] can be used on top of Golem95C.

3.2 Download and installation

QGRAF The program can be downloaded as Fortran source code from

<http://cfif.ist.utl.pt/~paulo/qgraf.html>.

After unpacking the tar-ball, a single Fortran77 file needs to be compiled.

FORM The program is available at

<http://www.nikhef.nl/~form/>

both as a compiled binary for many platforms and as a tar-ball. The build process, if built from the source files, is controlled by Autotools.

SAMURAI and Golem95C These libraries are available as tar-balls and from subversion repositories at

<http://projects.hepforge.org/samurai/>

and

<http://projects.hepforge.org/golem/95/>

respectively. For the user's convenience we have prepared a package containing SAMURAI and Golem95C together with the integral libraries OneLoop [74], QCD-Loop [75] and FF [59]. The package `gosam-contrib-1.0.tar.gz` containing all these libraries is available for download from:

<http://projects.hepforge.org/gosam/>

GOSAM The user can download the code either as a tar-ball or from the subversion repository at

<http://projects.hepforge.org/gosam/>.

The build process and installation of GOSAM is controlled by Python Distutils, while the build process for the libraries SAMURAI and Golem95C is controlled by Autotools.

Therefore the installation proceeds in two steps:

1. For all components which use Autotools, the following sequence of commands installs them under the user defined directory MYPATH.

```
./configure --prefix=MYPATH
make FC=gfortran F77=gfortran
make install # or sudo make install
```

If the configure script is not present, the user needs to run `sh ./autogen.sh` first.

2. For GOSAM which is built using Distutils, the user needs to run

```
python setup.py install \
    --prefix MYPATH
```

If MYPATH is different from the system default (e.g. `/usr/bin`), the environment variables `PATH`, `LD_LIBRARY_PATH` and `PYTHONPATH` might have to be set accordingly. For more details we direct the user to the GOSAM reference manual and to the documentation of the beforementioned programs.

4 Using GOSAM

4.1 Setting up a simple process

GOSAM is a very flexible program and comes with a wide range of configuration options. Not all of these options are relevant for simple processes and often the user can leave most of the settings at their default values. In order to generate the code for a process, one needs to prepare an input file, which will be called *process card* in the following, which contains

- process specific information, such as a list of initial and final state particles, their helicities (optional) and the order of the coupling constants;
- scheme specific information and approximations, such as the regularisation and renormalisation schemes, the underlying model, masses and widths which are set to zero, the selection of subsets of diagrams; the latter might be process dependent;
- system specific information, such as paths to programs and libraries or compiler options;
- optional information for optimisations which control the code generation.

In the following we explain how to set up the required files for the process $q\bar{q} \rightarrow gZ^0 \rightarrow ge^-e^+$. The example computes the QCD corrections for the $u\bar{u}$ initial state, where $m_e = 0$ and $N_f = 5$ massless quarks are assumed. For our example, we follow an approach where we keep the different types of information in separate files—`process.rc`, `scheme.rc` and `system.rc`—and use GOSAM to produce a process card for this process based on these files. This is not required—one could also produce and edit the process card directly—it is however more convenient to store system specific information into a separate, re-usable file, and it makes the code generation more transparent.

Process specific information The following listing contains the information which is specific to the process. The syntax of process cards requires that no blank character is left between the equals sign and the property name. Commentary can be added to any line, marked by the '#' character. Line continuation is achieved using a backslash at the end of a line.⁵

Listing 1 File 'process.rc'

```
1 process_path=qgqz
2 in=u,u~
3 out=g,e-,e+
4 helicities=++++, +---, -++-, -+--
5 order=QCD,1,3
```

⁵The line numbers are just for reference and should not be included in the actual files.

The first line defines the (relative) path to the directory where the process files will be generated. GOSAM expects that this directory has already been created. Lines 2 and 3 define the initial and final state of the process in terms of field names, which are defined in the model file. Besides the field names one can also use PDG codes [76, 77] instead. Hence, the following lines would be equivalent to lines 2 and 3 in Listing 1:

```
2 in=2,-2
3 out=21,11,-11
```

Line 4 describes the helicity amplitudes which should be generated. If no helicities are specified, the program defaults to the generation of all possible helicity configurations, some of which may turn out to be zero. The different helicity amplitudes are separated by commas; within one helicity amplitude there is one character (usually '+', '-' and '0') per external particle from the left to the right. In the above example for the reaction

$$u(k_1, \lambda_1)\bar{u}(k_2, \lambda_2) \rightarrow g(k_3, \lambda_3)e^-(k_4, \lambda_4)e^+(k_5, \lambda_5)$$

we have the following assignments:

Helicity	λ_1	λ_2	λ_3	λ_4	λ_5
0	+	-	+	-	+
1	+	-	-	-	+
2	-	+	+	-	+
3	-	+	-	-	+

With the above value for helicities we generate all non-vanishing helicities for the partons but keep the lepton helicities fixed. In more complicated examples this way of listing all helicities explicitly can be very tedious. Therefore, we introduced the option to generate sets of helicities using square brackets. For example, if the gluon helicity is replaced by $[+-]$, the bracket is expanded automatically to take the values $+$, $-$.

```
4 helicities=+-[+-]-+, -+[+-]-+
```

A further syntactical reduction can be achieved for the quarks. The current expansion of a square bracket and its opposite value can be assigned to a pair of variables as in $[xy=+-]$. If the bracket expands to '+' then x is assigned '+' and y is assigned the opposite sign, i.e. '-'. If the bracket expands to '-' the assignments are $x=-$ and $y=+$. Hence, the helicity states of a massless quark anti-quark pair are generated by $[qQ=+-]Q$, and the selection of helicities in our example can be abbreviated to

```
4 helicities=[qQ=+-]Q[+-]-+
```

which is equivalent to the version of this line in Listing 1.

Finally, the order (power) of the coupling constants has to be specified. Line 5 contains a keyword for the type of coupling (QCD or QED), the order of this coupling constant in the unsquared tree level amplitude (in our example: 1) and the order of the coupling constant in the unsquared one-loop amplitude (in our example: 3). One can also use GOSAM to generate the tree level only, by giving only the power of the tree level amplitude:

```
5 order=QCD, 1
```

Conversely, GOSAM will generate the virtual amplitude squared for processes where no tree level is present if the tree level order is replaced by the keyword NONE.

```
5 order=QCD, NONE, 3
```

Up to now, the file would generate all 8 tree level and 180 one-loop diagrams contributing to the process $u\bar{u} \rightarrow g e^- e^+$, regardless of the intermediate states. Nevertheless, what we intended to generate were only those diagrams where the electron pair comes from the decay of a $Z \rightarrow e^- e^+$. GOSAM offers two ways of achieving this diagram selection, either by passing a condition to QGRAF or by applying a filter written in Python. The first option would be specified by the option `qgraf.verbatim`, which copies the argument of the option to the QGRAF input file in verbatim. The following filter demands the appearance of exactly one Z-propagator, leaving us with 2 tree-level and 45 one-loop diagrams:

```
6 qgraf.verbatim= true=iprop[Z,1,1];
```

The alternative solution is the application of a Python filter using the options `filter.lo` for tree level and `filter.nlo` for one-loop diagrams. The current example requires the two lines

```
6 filter.lo= IPROP([Z])==1
7 filter.nlo= IPROP([Z])==1
```

Scheme specific information For our example we put all scheme specific definitions in the file `scheme.rc`. It contains the choice of a suitable regularisation scheme and fixes what types of UV counterterms are included in the final result.

Listing 2 File ‘`scheme.rc`’

```
1 extensions=dred
2 qgraf.options=onshell
3 zero=mU, mD, mC, mS, mB, me, wT
4 one=gs
```

In Listing 2, line 1 selects dimensional reduction as a regularisation scheme. If `dred` is not specified in the list of extensions, GOSAM works in the ‘tHooft Veltman scheme by default. Line 2 removes all on-shell bubbles on external legs. This is, on the one hand, required to be consistent with the renormalisation scheme. On the other hand, those diagrams would lead to zero denominators at the algebraic level. In line 3 all light quark masses, the mass of the electron and the width of the top quark are set to zero. Further, as a convention rather than a scheme, the strong coupling g_s is set to one in line 4, which means that g_s will not occur in the algebraic expressions, assuming that the user will multiply the final result by his desired value for the strong coupling. If the option `one=gs` is not used, the default value contained in the file `common/model.f90` will be used. This default value of course can be changed by the user.

System specific information In order to adapt the code generation to the system environment, GOSAM needs to find a way of determining all relevant paths and options for the programs and libraries used during generation, compilation and linking of the code. Those settings are fixed in the file `system.rc` in our example.⁶

Listing 3 File ‘`system.rc`’

```
1 system.extensions=samurai,golem95
2 samurai.fcflags=\
3   -I${PREFIX}/include/samurai
4 samurai.ldflags=\
5   -L${PREFIX}/lib -lsamurai
6 samurai.version=2.1.1
7 golem95.fcflags=\
8   -I${PREFIX}/include/golem95
9 golem95.ldflags=\
10  -L${PREFIX}/lib -lgolem95
11 form.bin=${PREFIX}/bin/tform
12 qgraf.bin=${PREFIX}/bin/qgraf
13 fc.bin=gfortran
```

Generating the code After having prepared the input files correctly we need to collect the information distributed over the three files `process.rc`, `scheme.rc` and `system.rc` in one input file, which we will call `gosam.in` here. The corresponding command is:

```
gosam.py --template gosam.in \
  --merge process.rc \
  --merge scheme.rc --merge system.rc
```

⁶In this example we assume that the user has defined an environment variable `PREFIX`.

The generated file can be processed with `gosam.py` directly but requires the process directory to be present.

```
mkdir qggz
gosam.py gosam.in
cd qggz
```

All further steps are controlled by the generated make files; in order to generate and compile all files relevant for the matrix element one needs to invoke

```
make compile
```

The generated code can be tested with the program `matrix/test.f90`. The following sequence of commands will compile and run the example program.

```
cd matrix
make test.exe
./test.exe
```

The last lines of the program output should look as follows⁷

```
#          LO:  0.3450350717601E-06
# NLO, finite part -10.77604823456547
# NLO, single pole -19.98478948141949
# NLO, double pole -5.6666666665861926
# IR,  single pole -19.98478948439310
# IR,  double pole -5.6666666666666666
```

The printed numbers are, in this order, a_0 , c_0/a_0 , c_{-1}/a_0 , c_{-2}/a_0 and the pole parts calculated from the infrared insertion operator [78, 79].

One can generate a visual representation of all generated diagrams using the command

```
make doc
```

which generates the file `doc/process.ps` using a Python implementation of the algorithm described in [60] and the L^AT_EX package AXODRAW [61].

4.1.1 Further options

GOSAM provides a range of options which influence the code generation, the compilation and the numerical evaluation of the amplitude. Giving an exhaustive list of all options would be far beyond the scope of this article and the interested user is referred to the reference manual. Nonetheless, we would like to point out some of GOSAM's capabilities by presenting the corresponding options.

⁷The actual numbers depend on the random number generator of the system because the phase space point is generated randomly; however, the pole parts should agree between the matrix element and the infrared insertion operator given that the matrix element is fully renormalised.

Generating the R_2 term When setting up a process the user can specify if and how the R_2 term of the amplitude should be generated by setting the variable `r2` in the setup file.

```
r2=explicit
```

Possible options for `r2` are `implicit`, which is the default, `explicit`, `off` and `only`. The keyword `implicit` means that the R_2 term is generated along with the four-dimensional numerator as a function in terms of \hat{q} , μ^2 and ε and is reduced at runtime by sampling different values for μ^2 . This is the slowest but also the most general option. Using the keyword `explicit` carries out the reduction of terms containing μ^2 or ε during code generation (see Appendix B). The keyword `off` puts the R_2 term to zero which is useful if the user wants to provide his own calculation for these terms. Conversely, using `r2=only` discards everything but the R_2 term (reducing it as in the case `explicit`) and puts GOSAM in the position of providing R_2 terms for external codes which work entirely in four dimensions.

Diagram selection GOSAM offers a two-fold way of selecting and discarding diagrams. One can either influence the way QGRAF generates diagrams or apply filters to the diagrams after they have been generated by QGRAF or combine the two methods. Let us assume that in the above example we want to remove the third generation of quarks completely. Hence, all closed quark loops would be massless and therefore the second generation is just an exact copy of the first one. We can therefore restrict the generation of closed quark loops to up and down quarks. GOSAM has a filter precisely for this purpose, which takes the field names of the flavours to be generated as arguments.

```
filter.nlo=NFGEN(U,D)
```

This filter can be combined with the already existing filter selecting only diagrams containing a Z-propagator using the AND function:

```
filter.nlo=AND( NFGEN(U,D), \
               IPROP([Z]) == 1 )
```

A further feature of the code generated by GOSAM is the possibility of selecting diagrams at runtime. For example, we would like to distinguish at runtime three different gauge invariant sets of diagrams at one-loop level:

1. diagrams with a closed quark loop where the Z is attached to the loop;
2. diagrams with a closed quark loop where the Z is emitted from the external quark line;
3. diagrams without a closed quark loop.

In order to provide the code for a diagram selection at runtime one simply replaces the above filter by a list of filters as follows

```
filter.nlo=[\
  AND( NFGEN(U,D), IPROP([Z]) == 1, \
    NF, LOOPVERTICES([Z],_,_) == 1), \
  AND( NFGEN(U,D), IPROP([Z]) == 1, \
    NF, LOOPVERTICES([Z],_,_) == 0), \
  AND( NFGEN(U,D), IPROP([Z]) == 1, \
    NOT(NF) ) ]
```

The two new filters in use are NF which selects closed quark loops only and LOOPVERTICES which counts the number of vertices attached to the loop with the given sets of fields running through the vertex (where $_$ replaces any field). In the Fortran files one can access the diagram selection through the routine `update_flags`. The three selection criteria are stored in a derived data type `virt_flags` which has fields `eval_0`, ..., `eval_2`, in general ranging from zero to the length of the list given in `filter.nlo`.

```
use groups
type(virt_flags) :: flags
flags%eval_0=.true. !first group only
flags%eval_1=.false.
flags%eval_2=.false.
call update_flags(flags)
```

Additional extensions Some of GoSAM's functionality is available through the `extensions` variable. On top of the already presented options for selecting a regularisation scheme (by adding the option `dred`) or for activating interfaces to several different reduction libraries (`samurai`, `golem95`, `pjfry`) the user can also add the following options:

`fr5` adds and activates the relevant code for the computation of the finite renormalisation of γ_5 required in the 't Hooft Veltman scheme as described in (32).

`powhegbox` generates routines for the computation of the color and spin correlated Born matrix elements as required by POWHEG [34].

`autotools` uses make files which use Autoconf and Automake for compilation of the matrix element.

`gaugecheck` replaces the polarisation vectors of external vector fields by

$$\epsilon^\mu(k_i) \rightarrow \epsilon^\mu(k_i) + z_i k_i^\mu \quad (35)$$

where the variable z_i defaults to zero and is accessible in the Fortran code through the symbol `gaugeiz`.

4.2 Interfacing the code

The matrix element code generated by GoSAM provides several routines to transparently access partial or full results of the amplitude calculation. Here, we only present a minimal set of routines which can be used to obtain the set of coefficients $[a_0, c_0, c_{-1}, c_{-2}]$ for a given scale and a given set of external momenta. The routines, which can be accessed through the modules `matrix`⁸ are defined as follows:

initgolem This subroutine must be called once before the first matrix element evaluation. It initializes all dependent model parameters and calls the initialisation routines of the reduction libraries.

```
subroutine initgolem(init_libs)
  use config, only: ki
  logical, optional, &
    & intent(in) :: init_libs
  end subroutine
end interface
```

The optional argument `init_libs` can usually be omitted. It should be used only when several initialisation calls become necessary, but the reduction libraries and loop libraries should be initialized only once. All model parameters are accessible as global variables in the module `model` and should be modified (if at all) before calling `initgolem`.

samplitude This subroutine starts the actual calculation of the amplitude for a given phase space point.

```
subroutine samplitude &
  & (vecs, scale2, amp, ok, h)
  use config, only: ki
  use kinematics, only: num_legs
  real(ki), dimension(num_legs,4), &
    & intent(in) :: vecs
  double precision, &
    & intent(in) :: scale2
  double precision, &
    & intent(out) :: amp
  logical, optional, &
    & intent(out) :: ok
  integer, optional, &
    & intent(in) :: h
  end subroutine
end interface
```

⁸If a process name was given all modules are prefixed by the name, e.g. if `process_name=pr01`, the module `matrix` would be renamed into `pr01_matrix`.

The first mandatory arguments of this routine are the external momenta `vecs`, where `vecs(i, :)` contains the momentum of the i -th particle as a vector $[E_i, p_i^x, p_i^y, p_i^z]$, and we use in-out kinematics, i.e. $p_1 + p_2 \rightarrow p_3 + \dots + p_N$. Maximal numerical stability is achieved if the beam axis is chosen along the z -axis. The second argument, `scale2 = μ_R^2` , is the square of the renormalisation scale. As a third argument the routine expects a vector which accepts the result in the format $[a_0, c_0, c_{-1}, c_{-2}]$ with the coefficients being defined in (24) and (25). The optional argument `ok` may be used in order to report the outcome of the reconstruction tests in `samurai` if no rescue method has been chosen (see Sect. 2.4.2). The last argument allows one to select a single helicity subamplitude; the index `h` runs from zero to the number of helicities minus one. The labeling of the helicities is documented for each process in the file `doc/process.ps`.

exitgolem This routine should be called once after the last amplitude evaluation in the program. It closes all open log files and gracefully terminates the reduction and loop libraries.

```
subroutine exitgolem(exit_libs)
  use config, only: ki
  logical, optional,
  &          intent(in) :: exit_libs
  end subroutine
end interface
```

The optional argument `exit_libs` should only be set if multiple calls to this routine (e.g. for different matrix elements) are necessary and the dependent libraries should be terminated only once.

A small program which computes the amplitude for a set of phase space points is automatically generated with the amplitude code in the file `test.f90` in the subdirectory `matrix`. The script `config.sh` in the `process` directory returns suitable compilation and linking options for the generated matrix element code.

4.3 Using the BLHA interface

The so-called *Binoth Les Houches Accord* (BLHA) [56] defines an interface for a standardized communication between one-loop programs (OLP) and Monte Carlo (MC) tools. The communication between the two sides is split into two main phases: an initialisation phase and a runtime phase. During initialisation the two programs establish an agreement by exchanging a set of files and typically initiate the code generation. The OLP runtime code is then linked to the MC program and, during the runtime phase, called through a well-defined set of routines providing NLO results for the phase

space points generated by the MC. According to this standard, it is the responsibility of the MC program to provide results for the Born matrix element, for the real emission and for a suitable set of infrared subtraction terms. A schematic overview on this procedure is shown in Fig. 4.

GOSAM can act as an OLP in the framework of the BLHA. In the simplest case, the MC writes an order file—in this example it is called `olp_order.lh`—and invokes the script `gosam.py` as follows:

```
gosam.py --olp olp_order.lh
```

Further, GOSAM specific options can be passed either in a file or directly at the command line. One can, for example, use `autotools` for the compilation by modifying the above line as follows.

```
gosam.py --olp olp_order.lh \
  extensions=autotools
```

The contract file is given the extension `.olc` by default and would be `olp_order.olc` in this example. Alternatively, the name can be altered using the `-o` option.

If successful, the invocation of `gosam.py` generates a set of files which can be compiled as before with a generated make file. The BLHA routines are defined in the Fortran module `olp_module` but can also be accessed from C programs.⁹ The routines `OLP_Start` and `OLP_EvalSubProcess` are defined exactly as in the BLHA proposal [56]. For convenience, we extended the interface by the functions `OLP_Finalize()`, which terminates all reduction libraries, and `OLP_Option(char*, int*)`, which can be used to pass non-standard options at runtime. For example, a valid call in C to adjust the Higgs mass would be

```
int ierr;
OLP_Options("mH=146.78", &ierr);
```

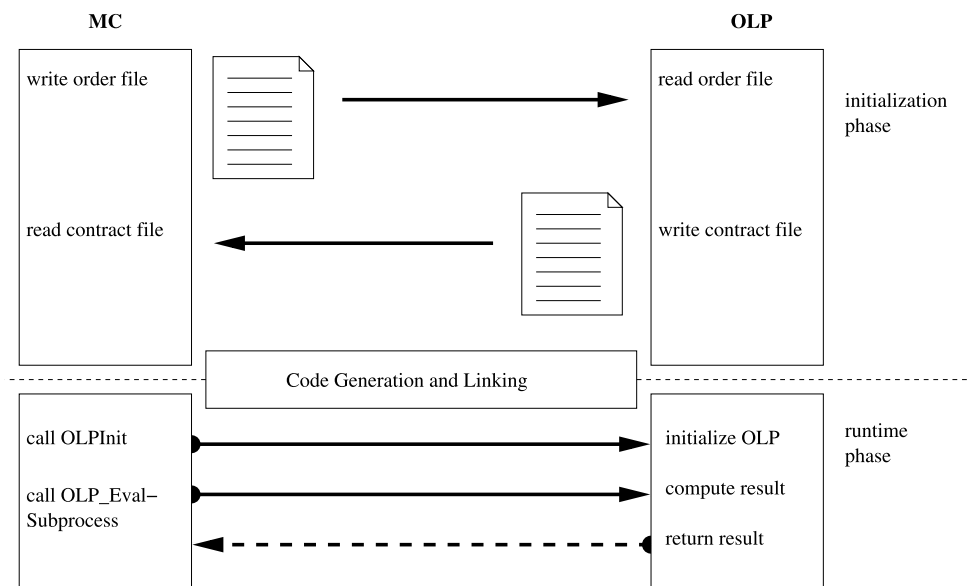
A value of one in `ierr` indicates that the setting was successful. A value of zero indicates an error.

4.4 Using external model files

With a few modifications in the process description files, GOSAM can immediately make use of model files generated by either `FeynRules` [80] in the UFO format [54] or by `LanHEP` [55]. In both cases, the following limitations and differences with respect to the default model files, `sm` and `smdiag`, apply:

⁹A header file is provided in `olp.h`.

Fig. 4 Schematic overview over the interaction between Monte Carlo tool and one-loop program in the Binoth Les Houches Accord



- As usual, particles can be specified by their PDG code. The field names, as used by QGRAF, are `parti` and `antii` for the particles with the PDG code i and $-i$ respectively. For example, the W^+ and the W^- boson would be called `part24` and `anti24`.
- All model parameters are prefixed by the letters `mdl` in order to avoid name clashes with existing variable names in the matrix element code.
- The variable `model.options` and the extension `fr5` are not guaranteed to work with models other than the built-in models.

Importing models in the UFO format A model description in the UFO format consists of a Python package stored in a directory. In order to import the model into GOSAM one needs to set the `model` variable in the input card to specify the keyword `FeynRules` in front of the directory name, where we assume that the model description is in the directory `$HOME/models/MSSM_UFO`.

```
model=FeynRules,$HOME/models/MSSM_UFO
```

Importing models in the LanHEP format LanHEP model descriptions consist of a set of plain text files in the same directory with a common numbering (such as `func4.mdl`, `lgrng4.mdl`, `prtcls4.mdl`, `vars4.mdl`). A LanHEP model can be loaded by specifying the path and the common number in the `model` variable. Assuming the files are situated in the directory `$HOME/models/MSSM_LHEP` one would set the variable as follows.

```
model=$HOME/models/MSSM_LHEP,4
```

Details about the allowed names for the table columns are described in the GOSAM reference manual. Precompiled `MSSM_UFO` and `MSSM_LHEP` files can also be found in the subdirectory `examples/model`.

5 Sample calculations and benchmarks

The codes produced by GOSAM have been tested on several processes. In this section we describe some examples of applications. Additional results, whose corresponding code is also included in the official distribution of the program, will be reported in Appendix B.

5.1 $pp \rightarrow W^- + j$ with SHERPA

In Sect. 4.3 the BLHA interface of GOSAM was presented. This interface allows one to link the program to a Monte Carlo event generator, which is, in general, responsible for supplying the missing ingredients for a complete NLO calculation of a physical cross section. Among the different general purpose Monte Carlo event generators, SHERPA [81] is one of those which offers these tools: computing the LO cross section, the real corrections with both the subtraction terms and the corresponding integrated counterparts [82–84]. Furthermore, SHERPA offers the possibility to match a NLO calculation with a parton shower [85, 86]. Using the BLHA interface, we linked GOSAM with SHERPA to compute the physical cross section for $W^- + 1$ jet at NLO.

The first steps to perform this linking is to write a SHERPA input card for the desired process. Instructions and many examples on how to write this can be found in the on-line

manual [87]. Running the code for the first time will produce an order file *OLE_order.lh* which contains all the necessary information for GOSAM, to produce the desired code for the loop part of the process. This includes a list of all partonic subprocesses needed. In parallel to the production of the needed SHERPA libraries with the provided script, one can at this point run the `gosam.py` command with the flag `-olp` and the correct path to the order file as explained in Sect. 4.3. Further options may be specified. Among them it is useful to have a second, GOSAM-specific, input card with all the important GOSAM options. Since, at the end, SHERPA needs to be linked to a dynamic library, it is convenient to run GOSAM with the *autotools* extension, which allows the direct creation of both static and dynamic libraries, together with the test routine *test*. The `gosam.py` script creates all the files needed for interfacing GOSAM with the Monte Carlo event generator together with the code for the one-loop computation of all needed subprocesses, and a makefile to run them. The different parton-level subprocesses are contained in different subdirectories. At this point the user simply has to run the makefile to generate and compile the code. Once the one-loop part of the code is ready, the produced shared library must be added to the list of needed libraries in the SHERPA input card as follows.

```
SHERPA_LDADD = LHOLE golem_olp;
```

With this operation the generation of the code is completed. The evaluation of the process and the physical analysis can then be performed at the user's discretion following the advice given in the SHERPA on-line documentation [87].

We tested the BLHA interface by computing $W^- + 1$ jet and producing distributions for several typical observables.

In Figs. 5(a) and 5(b) the inclusive transverse momentum and rapidity of the jets is shown. These distributions were compared with similar ones produced using the program MCFM [27, 28], and perfect agreement was found.

5.2 $pp \rightarrow W^\pm + j$, EW corrections

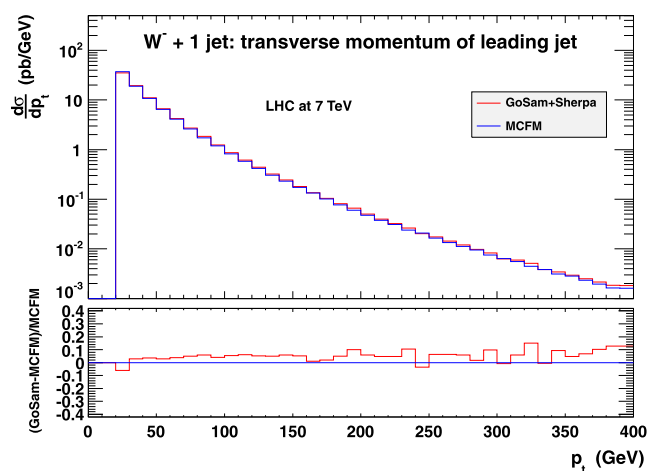
As a first example of an electroweak calculation, we computed the virtual one-loop corrections to $u\bar{d} \rightarrow Wg$. A complete analytical calculation for this process was presented in Ref. [88].

parameters			
M_Z	91.1876	M_W	80.419
$\cos\theta_w$	0.88156596117995394232	μ	M_W

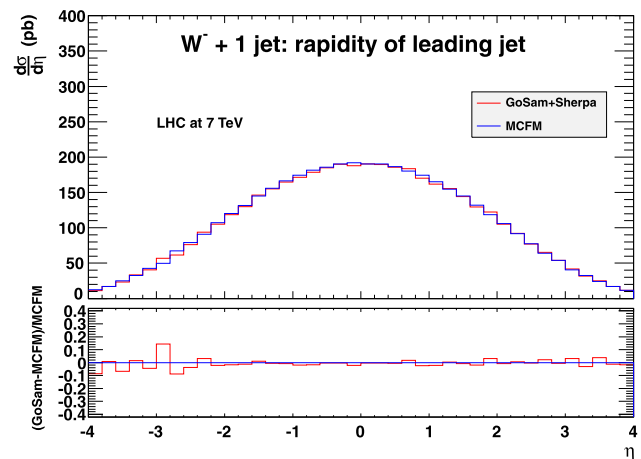
For the kinematic point given in Table 2 and the above parameters we obtain the following result:

result $u\bar{d} \rightarrow Wg$			
a_0	2.812364835883295		
c_0/a_0 unren.	-94.52525523327047		
c_{-1}/a_0 unren.	17.84240236996827		
c_{-2}/a_0 unren.	-0.5555555555555560		
renormalized			
	GOSAM	(67, 70) of Ref. [88]	
c_{-1}/a_0	4.743825167813529	4.7438251678146885	
c_{-2}/a_0	-0.5555555555555560	-0.5555555555555555	

The poles have been renormalized using (49)–(64) in Sects. 3.3 and 3.4 of [88]. Our result is agreement with (67), (70) of Ref. [88] and with Ref. [89] for the infrared divergences that remain after renormalisation.



(a) Inclusive transverse momentum of the leading jet for $W^- + 1$ jet production at LHC with $\sqrt{s} = 7$ TeV.



(b) Inclusive pseudorapidity of the leading jet for $W^- + 1$ jet production at LHC with $\sqrt{s} = 7$ TeV.

Fig. 5 NLO calculation of $W^- + 1$ jet production at LHC using GOSAM interfaced with SHERPA via the BLHA interface. The comparison to MCFM is also shown

Table 2 Kinematic point used in $pp \rightarrow W^\pm + j$, EW

	E	p_x	p_y	p_z
u	500	0	0	500
\bar{d}	500	0	0	500
W	503.23360778049988	110.20691318538486	441.95397288433196	-198.26237811718670
g	496.76639221950012	-110.20691318538488	-441.95397288433202	198.26237811718664

5.3 $\gamma\gamma \rightarrow \gamma\gamma$

The process $\gamma\gamma \rightarrow \gamma\gamma$ in the Standard Model first arises at the one-loop order, and proceeds through a closed loop of fermions and W bosons. Of the 16 helicity amplitudes contributing to it, only three are independent and their analytic expressions can be found in [90]. The pure QED contribution, involving a fermion loop, is contained in `samurai-1.0` [40] and will not be repeated here. Instead, we show the results of the W -loop contribution to the independent helicity amplitudes, as an example of EW corrections that can be handled with `GOSAM`.

parameters			
\sqrt{s}	1000	μ	\sqrt{s}
M_W	80.376	e	1

With the above parameters and the kinematics of Table 3 we obtain the following results.

result $\gamma\gamma \rightarrow \gamma\gamma$ (EW)		
	<code>GoSAM (dred)</code>	Refs. [90]
$ \mathcal{M}_{++++} $	12.02541904626610	12.025419045962
$ \mathcal{M}_{++--} $	7.380406043429961	7.3804060437434
$ \mathcal{M}_{+-+-} $	982.7804939723322	982.78049397093

5.4 $pp \rightarrow \chi_1^0 \chi_1^0$ in the MSSM

As an example for the usage of `GoSam` with a model file different from the Standard Model we calculated the QCD

corrections to neutralino pair production in the MSSM. The model file has been imported via the interface `UFO` (Universal FeynRules Output) [54] which facilitates the import of Feynman rules generated by `FeynRules` [80] to programs generating one-loop amplitudes. To import such files within the `GoSam` setup, all the user has to do is to give the path to the corresponding model file in the input card.

For this example, we combined the one-loop amplitude with the real radiation corrections to obtain results for differential cross sections. A calculation of neutralino pair production for the LHC presenting total cross sections at NLO is given in [91].

For the infrared subtraction terms the program `Mad-Dipole` [92, 93] is used, the real emission part is calculated using `MadGraph/MadEvent` [94]. The virtual matrix element is renormalized in the \overline{MS} scheme, while massive particles are treated in the on-shell scheme. The renormalisation terms specific to the massive MSSM particles have been added manually.

In Fig. 6 we show the differential cross section for the $m_{\chi_1^0 \chi_1^0}$ invariant mass, where we employed a jet veto to suppress large contributions from the channel $qg \rightarrow \chi_1^0 \chi_1^0 q$ which opens up at order $\alpha^2 \alpha_s$, but for large p_T^{jet} belongs to the distinct process of neutralino pair plus one hard jet production at leading order. We used $N_f = 5$ massless quark flavours and the MSTW08 [95] parton distribution functions. For the SUSY parameters we use the modified benchmarks point `SPS1amod` suggested in [96], and we use $\sqrt{s} = 7$ TeV.

For reference, we also give the result for the unrenormalised amplitude at one specific phase space point for $u\bar{u} \rightarrow \chi_1^0 \chi_1^0$ in the DRED scheme, using the following parameters and momenta:

Table 3 Kinematic point used in $\gamma\gamma \rightarrow \gamma\gamma$

	E	p_x	p_y	p_z
γ	500	0	0	500
γ	500	0	0	-500
γ	500	436.6186300198938284	-59.1784256571505765	236.3516148798047425
γ	500	-436.6186300198938284	59.1784256571505765	-236.3516148798047425

parameters			
M_Z	91.1876	Γ_Z	0
M_W	79.829013	$\sin^2 \theta_w$	$1 - M_W^2/M_Z^2$
μ	M_Z	N_f	1
g_s	1	α_w^{-1}	127.934
$M_{\chi_1^0}$	96.6880686	$M_{\tilde{g}}$	607.713704
$M_{\tilde{u}_L}$	561.119014	$M_{\tilde{u}_R}$	549.259265
M_{h_0}	110.899057	M_{H_0}	399.960116

All widths have been set to zero; for further settings we refer to the model parameter files contained in the subdirectory `examples/model/MSSM_UFO`. We have checked that the pole terms of the renormalised amplitude cancel with the infrared poles from MadDipole. For the phase

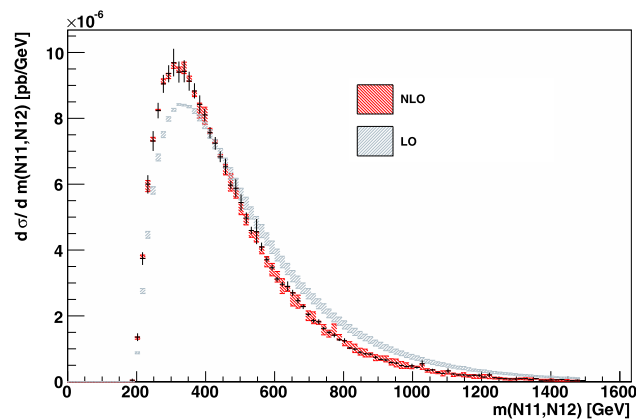


Fig. 6 Comparison of the NLO and LO $m_{\chi_1^0 \chi_1^0}$ distributions for the process $pp \rightarrow \chi_1^0 \chi_1^0$ with a jet veto on jets with $p_T^{\text{jet}} > 20$ GeV and $\eta < 4.5$. The band gives the dependence of the result on $\mu = \mu_F = \mu_R$ between $\mu_0/2$ and $2\mu_0$. We choose $\mu_0 = M_Z$. The black line gives the bin error for the value at the central scale

Table 4 Kinematic point used in $pp \rightarrow \chi_1^0 \chi_1^0$ in the MSSM

	E	p_x	p_y	p_z
u	1000	0	0	1000
\bar{u}	1000	0	0	-1000
χ_1^0	1000	42.3752677206678996	115.0009952646289548	987.7401101322898285
χ_1^0	1000	-42.3752677206678996	-115.0009952646289548	-987.7401101322898285

Table 5 Kinematic point used in $e^+e^- \rightarrow e^+e^-\gamma$

	E	p_x	p_y	p_z
e^+ (in)	0.5	0	0.4999997388800458	0
e^- (in)	0.5	0	-0.4999997388800458	0
e^+ (out)	0.1780937847558600	0.1279164180985903	0.05006809884093004	0.1133477415216646
e^- (out)	0.3563944406457374	0.02860530642319879	0.1832142729949070	0.3043534176228102
γ	0.4655117745984024	0.1565217245217891	0.1331461741539769	0.4177011591444748

space point given in Table 4 we obtain the following numbers.

GoSAM result $u\bar{u} \rightarrow \chi_1^0 \chi_1^0$	
a_0	$0.8680577964243597 \cdot 10^{-3}$
c_0/a_0	-31.9136615197871
c_{-1}/a_0	13.4374663711899
c_{-2}/a_0	2.66666666666667

5.5 $e^+e^- \rightarrow e^+e^-\gamma$

As an example of a QED calculation, we compared the virtual QED corrections for the process $e^+e^- \rightarrow e^+e^-\gamma$ with the results provided in [97]. The results compared in the table are the bare unrenormalised amplitudes in the 't Hooft Veltman scheme. No counterterms or subtraction terms have been added to the result.

parameters			
\sqrt{s}	1.0	α	$7.2973525376 \cdot 10^{-3}$
μ	\sqrt{s}	m_e	$0.51099891 \cdot 10^{-3}$

Using the parameters given above and the kinematics of Table 5 we obtain the following results.

result $e^+e^- \rightarrow e^+e^-\gamma$		
	GoSAM	Ref. [97]
a_0	0.7586101468103622	0.7586101468103619
c_0/a_0	0.5005827938274887	0.5005828268263969
c_{-1}/a_0	0.0474506407008029	0.0474506427003504
c_{-2}/a_0	0	0

5.6 $pp \rightarrow t\bar{t}H$

This process has been compared with the results given in [39]. The partonic subprocesses $u\bar{u} \rightarrow t\bar{t}H$ and $gg \rightarrow t\bar{t}H$ were computed both in the 't Hooft Veltman scheme and in dimensional reduction and the fully renormalised results were successfully compared as an internal consistency check. Apart from wave function renormalisation and mass counterterms, Yukawa coupling renormalisation is also needed here. Yukawa coupling counterterms are in this case equal to the wave function counterterms. The Yukawa top mass is set equal to its pole mass.

parameters			
\sqrt{s}	500.0	N_f	5
μ	m_t	$N_{f,h}$	1
m_t	172.6	α_s	0.1076395107858145
m_H	130	v	246.21835258713082

The kinematics used to obtain the results below is given in Table 6. The results are given in the 't Hooft Veltman scheme, and are fully renormalised.

result $u\bar{u} \rightarrow t\bar{t}H$			
	GoSAM	Ref. [39]	
$a_0 \cdot 10^4$	2.200490364806190	2.2004904613782828	
c_0/a_0	-15.29615178164782	-15.29615211731521	
c_{-1}/a_0	-1.640361500121837	-1.640361536072381	
c_{-2}/a_0	-2.6666666666666666	-2.666666725182165	

Table 6 Kinematic point used in $pp \rightarrow t\bar{t}H$

	E	p_x	p_y	p_z
u/g	250.0	0.0	0.0	250.0
\bar{u}/g	250.0	0.0	0.0	-250.0
H	136.35582793693018	15.133871809486299	27.986733991031045	26.088703626953386
t	181.47665951104506	20.889486679044587	-50.105625289561424	14.002628607367491
\bar{t}	182.16751255202476	-36.023358488530903	22.118891298530357	-40.091332234320859

Table 7 Kinematic point used for $gg \rightarrow t\bar{t}Z$

	E	p_x	p_y	p_z
g	7000.0	0.0	0.0	7000.0
g	7000.0	0.0	0.0	-7000.0
t	6270.1855170414337	-4977.7694025303863	806.93726196887712	3725.2619580634337
\bar{t}	6925.5258180925930	5306.3374282745517	-1281.8763412410237	-4258.3185872039012
Z	804.28866486597315	-328.56802574416463	474.93907927214622	533.05662914046729

result $gg \rightarrow t\bar{t}H$

	GoSAM	Ref. [39]
$a_0 \cdot 10^5$	6.127399805961155	6.127400074872043
c_0/a_0	9.006680638719660	9.006680836410272
c_{-1}/a_0	2.986347664537282	2.9863477301662056
c_{-2}/a_0	-6.000000000000004	-6.000000131659877

On an Intel Core i7 950 at 3 GHz the evaluation of a single phase space point took 44 ms in the $u\bar{u}$ channel and 223 ms in the gg channel. The code was compiled with gfortran without optimisations.

5.7 $gg \rightarrow t\bar{t}Z$

This amplitude, fully renormalised, has been compared with the results given in [37].

parameters			
g_s	1	G_F	0.0000116639
μ	m_t	N_f	5
m_t	170.9	M_W	80.45
M_Z	91.18		

The kinematics used to obtain the results below is given in Table 7.

result $gg \rightarrow t\bar{t}Z$			
	GoSAM	Ref. [37]	
$a_0 \cdot 10^6$	0.1531395190212139	0.1531395190212831	
c_0/a_0	-204.9208290898557	-204.920829867328	
c_{-1}/a_0	50.62939646427283	50.6293965717156	
c_{-2}/a_0	-5.999999999999997	-6.000000000000003	

The evaluation of a single phase space point took 1433 ms on a 2 GHz processor. The code was compiled with `gfortran -O2`.

5.8 $pp \rightarrow b\bar{b}b\bar{b} + X$

A detailed discussion of this process can be found in [98, 99]. In this section we focus on the parts that are relevant in the context of the virtual corrections. In particular we compared our result to the one given in [38], which is the fully renormalised amplitude including the mass counterterms for the top-quark contribution.

parameters			
\sqrt{s}	500	N_f	5
μ	\sqrt{s}	$N_{f,h}$	1
m_t	174	m_b	0
Γ_t	0	g_s	1

The results below are obtained for the phase space point of Table 8 using the above parameters.

result $gg \rightarrow b\bar{b}b\bar{b}$			
	GoSAM	Ref. [38]	
$a_0 \cdot 10^6$	1.022839601391936	1.022839601391910	
c_0/a_0	-36.97653243659754	-36.97653243473214	
c_{-1}/a_0	-34.01491655155776	-34.01491655142099	
c_{-2}/a_0	-11.33333333333512	-11.33333333333343	

Table 8 Kinematic point used in $pp \rightarrow b\bar{b}b\bar{b}$

	E	p_x	p_y	p_z
u/g	250.0	0.0	0.0	250.0
\bar{u}/g	250.0	0.0	0.0	-250.0
b	147.5321146846735	24.97040523056789	-18.43157602837212	144.2306511496888
\bar{b}	108.7035966213640	103.2557390255471	-0.5484684659584054	33.97680766420219
b	194.0630765341365	-79.89596300367462	7.485866671764871	-176.6948628845280
\bar{b}	49.70121215982584	-48.33018125244035	11.49417782256567	-1.512595929362970

Table 9 Kinematic point used in $pp \rightarrow t\bar{t}b\bar{b}$

	E	p_x	p_y	p_z
u/g	250.0	0.0	0.0	250.0
\bar{u}/g	250.0	0.0	0.0	-250.0
t	190.1845561691092	12.99421901255723	-9.591511769543683	75.05543670827210
\bar{t}	182.9642163285034	53.73271578143694	-0.2854146459513714	17.68101382654795
b	100.9874727883170	-41.57664370692741	3.895531135098977	-91.94931862397770
\bar{b}	25.86375471407044	-25.15029108706678	5.981395280396083	-0.7871319108423604

result $u\bar{u} \rightarrow b\bar{b}b\bar{b}$		
	GoSAM	Ref. [38]
$a_0 \cdot 10^9$	5.753293428094349	5.753293428094391
c_0/a_0	-22.19223384585620	-22.19223384564902
c_{-1}/a_0	-20.89828996870689	-20.89828996857439
c_{-2}/a_0	-8.000000000000199	-8.000000000000037

On an Intel Xeon E7340 the running time for the calculation of a single phase space point was 19.6 s for the gluon initiated channel and 440 ms for the quark channel.

5.9 $pp \rightarrow t\bar{t}b\bar{b} + X$

This process has been compared with the results given in [38]. We have set up the process both in the 't Hooft Veltman scheme and in dimensional reduction and successfully compared the fully renormalised results as an internal consistency check. The results below are given in the 't Hooft Veltman scheme, and only the counterterms for $|\mathcal{M}|_{\text{ct},\delta m_t}^2$ are included.

parameters			
\sqrt{s}	500.0	N_f	5
μ	\sqrt{s}	$N_{f,h}$	1
m_t	174.0	m_b	0.0
Γ_t	0.0	g_s	1.0

Using the above parameters and the phase space point of Table 9 we obtain the following results.

result $u\bar{u} \rightarrow t\bar{t}b\bar{b}$		
	GoSAM	Ref. [38]
$a_0 \cdot 10^8$	2.201164677187755	2.201164677187727
c_0/a_0	8.880263116574282	8.880263117410131
c_{-1}/a_0	-4.730495922109534	-4.730495921691266
c_{-2}/a_0	-5.333333333333468	-5.333333333333190
result $gg \rightarrow t\bar{t}b\bar{b}$		
	GoSAM	Ref. [38]
$a_0 \cdot 10^8$	8.279470201927135	8.279470201927128
c_0/a_0	21.83922035777929	21.83922035648926
c_{-1}/a_0	-12.59181277770347	-12.59181277853837
c_{-2}/a_0	-8.666666666666764	-8.666666666666549

On an Intel Core i7 950 at 3 GHz the evaluation of a single phase space point took 393 ms in the $u\bar{u}$ channel and 12.3 s in the gg channel. The code was compiled with gfortran without optimisations.

5.10 $pp \rightarrow W^+W^-b\bar{b}$

The subprocesses $u\bar{u} \rightarrow W^+W^-b\bar{b}$ and $gg \rightarrow W^+W^-b\bar{b}$ have been calculated both in [38] and [39]. Accordingly, the results below are given in the 't Hooft Veltman scheme, where only the counterterms for $|\mathcal{M}|_{\text{ct},\delta m_t}^2$ are included.

parameters			
\sqrt{s}	500.0	N_f	5
μ	\sqrt{s}	$N_{f,h}$	1
m_t	174.0	m_b	0
Γ_t	0	g_s	1
M_Z	91.188	Γ_Z	2.44140351
M_W	80.419	Γ_W	0
$1/\alpha$	132.50686625		

With the above parameters and the kinematics defined in Table 10 we obtain the following results.

Table 10 Kinematic point used in $pp \rightarrow W^+W^-b\bar{b}$

	E	p_x	p_y	p_z
u/g	250.0	0.0	0.0	250.0
\bar{u}/g	250.0	0.0	0.0	-250.0
W^+	154.8819879118765	22.40377113462118	-16.53704884550758	129.4056091248114
W^-	126.4095336206695	92.64238702192333	-0.4920930146078141	30.48443210132545
b	174.1159068988160	-71.68369328357026	6.716416578342183	-158.5329205583824
\bar{b}	44.59257156863792	-43.36246487297426	10.31272528177322	-1.357120667754454

result $gg \rightarrow W^+W^-b\bar{b}$		
	GoSAM	Ref. [39]
$a_0 \cdot 10^8$	1.549796787502985	1.549795815702494
c_0/a_0	-17.80558461276584	-17.80558440908488
c_{-1}/a_0	-19.61125131175888	-19.611251301307803
c_{-2}/a_0	-8.666666666666668	-8.666666666666661
result $u\bar{u} \rightarrow W^+W^-b\bar{b}$		
	GoSAM	Ref. [39]
$a_0 \cdot 10^8$	2.338048681706755	2.338048676370483
c_0/a_0	-5.936151367348438	-5.936151368788066
c_{-1}/a_0	-10.44868110371249	-10.44868110378090
c_{-2}/a_0	-5.33333333333312	-5.33333333333336

5.11 $u\bar{d} \rightarrow W^+ggg$

The amplitude $u\bar{d} \rightarrow W^+ggg$ is an important channel in the calculation of the process $pp \rightarrow W^+ + 3$ jets. The QCD corrections to this process have been presented in Refs. [6–9].

The subprocess with one quark pair and three gluons consists of more than 1500 Feynman diagrams. We have computed the amplitude including the leptonic decay of the W -boson and compared our result to [38].

parameters			
\sqrt{s}	500.0	N_f	5
μ	\sqrt{s}	$N_{f,h}$	1
m_t	174.0	M_Z	91.188
$\Gamma_t, \Gamma_W, \Gamma_Z$	0.0	M_W	80.419
g_s	1.0	G_F	$1.16639 \cdot 10^{-5}$

Furthermore, the values for the dependent parameters are $\cos^2 \theta_W = M_W^2/M_Z^2$ and $\alpha = \sqrt{2}G_F M_W^2 \sin^2 \theta_W / \pi$. For the phase space point of Table 11 we obtain the numbers below.

result $u\bar{d} \rightarrow W^+ggg$		
	GoSAM	Ref. [38]
$a_0 \cdot 10^7$	8.552735739069321	
c_0/a_0	-36.45372625230239	-36.4536949986367
c_{-1}/a_0	-34.70010131004584	-34.70007155977844
c_{-2}/a_0	-11.66666666666747	-11.666656664302845

Table 11 Kinematic point used in $u\bar{d} \rightarrow W^+ ggg$

	E	p_x	p_y	p_z
u	250.0	0.0	0.0	250.0
\bar{d}	250.0	0.0	0.0	-250.0
W^+	162.5391101447744	23.90724239064912	-17.64681636854432	138.0897548661186
g	104.0753327455388	98.85942812363483	-0.5251163702879512	32.53017998659339
g	185.8004692730082	-76.49423931754684	7.167141557113385	-169.1717405928078
g	47.58508783667868	-46.27243119673712	11.00479118171890	-1.448194259904179

On an Intel Core 2 i5 Laptop at 2.0 GHz the evaluation of a single phase space point took about 2.5 s for $u\bar{d} \rightarrow e^+ \nu_e ggg$ and about 7.5 s for on-shell W 's without decay. The code was compiled with `gfortran -O2`.

5.12 $u\bar{d} \rightarrow W^+ (\rightarrow \nu_e e^+) b\bar{b}$ (massive b -quark)

The process $u\bar{d} \rightarrow W^+ b\bar{b}$, with an on-shell W -boson, has been studied in [100], while the effects of the W -decay have been recently accounted for in [101], and implemented within MCFM. We consider the latter process, and compare the renormalised amplitude evaluated by MCFM. The b -quark is treated as massive in all diagrams except in the vacuum-polarisation like contributions.

parameters			
μ	80.0	g_s	1
m_t	172.5	m_b	4.75
M_Z	91.1876	M_W	80.419
Γ_W	2.1054	G_F	0.0000116639
V_{ud}	0.975		

Using the above parameters and the kinematics given in Table 12 we obtain the following results.

Table 12 Kinematic point used in $u\bar{d} \rightarrow W^+ b\bar{b}$

	E	p_x	p_y	p_z
u	76.084349979114506	0.0	0.0	76.084349979114506
\bar{d}	1998.0331337409114	0.0	0.0	-1998.0331337409114
ν_e	-953.55303294091811	955.01676368653477	50.025808060592873	17.060211586132972
e^+	-190.20402007017753	194.22279012023398	4.3588877692445251	39.063065018596490
b	-417.39085287123652	468.23544715890415	208.22173996408185	40.625785184424117
\bar{b}	-360.80087787946474	456.64248275435313	-262.60643579391922	-96.749061789153586

result $u\bar{d} \rightarrow \nu_e e^+ b\bar{b}$

	GoSAM	MCFM-6.0
$a_0 \cdot 10^7$	1.884434667673654	1.88443466774536441
c_0/a_0	41.21712989438873	41.217129894410029
c_{-1}/a_0	26.60367070701196	
c_{-2}/a_0	-2.6666666666666624	
IR_{-1}	26.60367070701218	
IR_{-2}	-2.666666666666667	

The evaluation of a single phase space point took 9.12 ms on a 2 GHz processor. The code was compiled with `gfortran -O2`.

6 Conclusions

We have presented the program package GoSAM which produces, in a fully automated way, the code required to perform the evaluation of one-loop matrix elements for multi-particle processes. The program is publicly available at <http://projects.hepforge.org/gosam/> and can be used to calculate one-loop amplitudes within QCD, electroweak theory, or other models which can be imported via an interface to LanHEP and UFO, also included in the release. Monte Carlo programs for the real radiation can be easily linked through the BLHA interface.

GoSAM is extremely flexible, allowing for both unitarity-based reduction at integrand level and traditional tensor reduction, or even for a combination of the two approaches when required. The amplitudes are generated in

terms of Feynman diagrams within the dimensional regularisation scheme, and optionally the calculation can be carried out either in the 't Hooft Veltman or in the dimensional reduction variant. The user can choose among different libraries for the master integrals, and the setup is such that other libraries can be linked easily.

The calculation of the rational terms is very modular and can proceed either along with the same numerical reduction as the rest of the amplitude, or independently, before any reduction, by using analytic information on the integrals which can potentially give rise to a rational part. In the current version of the code, UV-renormalisation counterterms are provided for QCD corrections only. Further improvements concerning the full automatised of electroweak corrections are planned.

Different systems to detect and rescue numerical instabilities are implemented, and the user can switch between them without having to re-generate the source code. Due to a careful organisation of the calculation both at the code generation stage and at the reduction stage, the runtimes for multi-particle amplitudes are very satisfactory. Moreover, the GOSAM generator can also produce codes for processes that include intermediate states with complex masses.

Within the context of the automated matching of Monte Carlo programs to NLO virtual amplitudes, GOSAM can be used as a module to produce differential cross sections for multi-particle processes which can be compared directly to experiment. Therefore we believe that GOSAM can contribute to the goal of using NLO tools as a standard framework for the LHC data analysis at the TeV scale.

Acknowledgements We would like to thank the SHERPA collaboration for the support, in particular Jennifer Archibald, Frank Krauss and Marek Schönherr. We also would like to thank Rikkert Frederix, Adam Kardos, Stefano Pozzorini, Zoltan Trocsanyi, Thomas Schutzmeier and Christian Sturm for their input to various comparisons and clarifying discussions, and Edoardo Mirabella for important feedback on Samurai. G.C. and G.L. were supported by the British Science and Technology Facilities Council (STFC). The work of G.C. was supported by DFG Sonderforschungsbereich Transregio 9, Computergestützte Theoretische Teilchenphysik. N.G. was supported in part by the U.S. Department of Energy under contract No. DE-FG02-91ER40677. P.M. and T.R. were supported by the Alexander von Humboldt Foundation, in the framework of the Sofja Kovaleskaja Award Project “Advanced Mathematical Methods for Particle Physics”, endowed by the German Federal Ministry of Education and Research. The work of G.O. was supported in part by the National Science Foundation under Grant PHY-0855489 and PHY-1068550. The research of F.T. is supported by Marie-Curie-IEF, project: “SAMURAI-Apps”. We also acknowledge the support of the Research Executive Agency (REA) of the European Union under the Grant Agreement number PITN-GA-2010-264564 (LHCPhenoNet).

Open Access This article is distributed under the terms of the Creative Commons Attribution License which permits any use, distribution, and reproduction in any medium, provided the original author(s) and the source are credited.

Appendix A: Examples included in the release

In the following we give results for the processes listed in the `examples` directory. Unless stated otherwise, we assume that the coupling constants (e and g_s in the standard model) have been set to one in the input card. The conventions for the returned numbers (a_0, c_0, c_{-1}, c_{-2}) are as stated in Sect. 2.5. Dimensionful parameters are understood to be in powers of GeV.

As an illustration of the potential of GOSAM, we display in Table 13 the timings required by a wide list of benchmark processes. The first value provided in the table is the time required for the code generation (*Generation*, given in seconds): we remind the reader that this operation only needs to be performed once per process. The second value is the timing for the full calculation of the amplitude at one phase-space point (*Evaluation*, in milliseconds). Results are obtained with an Intel(R) Core(TM) i7 CPU 950 @ 3.07 GHz.

Table 13 Time required for code generation and calculation of one phase-space point. The results were obtained with an Intel(R) Core(TM) i7 CPU 950 @ 3.07 GHz. The time for the evaluation of a phase space point is taken as the average of the time obtained from the evaluation of 100 random points generated using RAMBO [102], where the code was compiled using `gfortran` without any optimisation options. The generation of the R_2 term was set to `explicit`

Process	Generation [s]	Evaluation [ms]
$bg \rightarrow Hb$	236	2.49
$d\bar{d} \rightarrow t\bar{t}$	341	4.71
$d\bar{d} \rightarrow t\bar{t}$ (DRED)	324	4.05
$dg \rightarrow dg$	398	3.08
$dg \rightarrow dg$ (DRED)	402	3.28
$e^+e^- \rightarrow t\bar{t}$	221	1.27
$e^+e^- \rightarrow t\bar{t}$ (LanHEP)	180	1.27
$e^+e^- \rightarrow u\bar{u}$	122	0.65
$gg \rightarrow gg$	525	1.69
$gg \rightarrow gg$ (DRED)	428	1.66
$gg \rightarrow gg$ (LanHep)	1022	1.70
$gg \rightarrow gZ$	529	15.18
$gg \rightarrow t\bar{t}$	1132	24.65
$gg \rightarrow t\bar{t}$ (DRED)	957	30.13
$gg \rightarrow t\bar{t}$ (UFO)	1225	29.45
$H \rightarrow \gamma\gamma$	140	0.24
$gb \rightarrow e^-\bar{\nu}_e t$	337	2.89
$u\bar{d} \rightarrow e^-\bar{\nu}_e$	71	0.09
$u\bar{d} \rightarrow e^-\bar{\nu}_e g$	154	1.15
$u\bar{u} \rightarrow d\bar{d}$	186	2.06
$\bar{u}d \rightarrow W^+W^+\bar{c}s$	1295	17.37
$\gamma\gamma \rightarrow \gamma\gamma$	597	6.08

A.1 How to run the examples

The example directories only define the system independent part of the setup. All settings which are defined in the file `system.rc` (see Sect. 4) must be put either in a file called `$HOME/.gosam` or in the file `setup.in` in the `GOSAM examples/` directory. A script `runtests.sh` is provided to generate, compile and run the test programs. The names of the directories respectively examples to be run should be specified at the command line, e.g.

```
./runtests.sh eeuu bghb
```

If the script is invoked without arguments it will loop over all subdirectories. A second script, `summarize.sh`, can be used in order to collect the test results and print a summary to the screen. The command

```
./summarize.sh
```

will produce an output like the following one.

```
+ bghb (succeeded)
+ eeuu (succeeded)
grep: ./ddtt/...: No such file ...
```

The examples $e^+e^- \rightarrow t\bar{t}$ have an explicit dependence on the Golem95C library and will therefore fail if the extension `golem95` is not added.

A.2 $e^+e^- \rightarrow u\bar{u}$

The following parameters and momenta have been used to produce the numerical result:

	E	p_x	p_y	p_z
e^+	E	0	0	E
e^-	E	0	0	$-E$
u	E	$E \sin \theta \sin \phi$	$E \sin \theta \cos \phi$	$E \cos \theta$
\bar{u}	E	$-E \sin \theta \sin \phi$	$-E \sin \theta \cos \phi$	$-E \cos \theta$

Table 14 Kinematic point used in $e^+e^- \rightarrow t\bar{t}$

	E	p_x	p_y	p_z
e^+	74.7646520969852	0	0	74.7646520969852
e^-	6067.88254935176	0	0	-6067.88254935176
t	5867.13826404309	16.7946967430656	169.437140279981	-5862.12966020487
\bar{t}	275.508937405653	-16.7946967430656	-169.437140279981	-130.988237049907

parameters

E	74.7646520969852	μ^2	$4 E^2$
ϕ	2.46	θ	1.35
M_Z	91.1876	Γ_Z	2.4952
M_W	$\cos \theta_w M_Z$	$\sin \theta_w$	0.47303762

result $e^+e^- \rightarrow u\bar{u}$

	GoSAM	analytic
a_0	3.7878306213027528	
c_0/a_0	$1.86960440108932 \times C_F$	$(\pi^2 - 8) \times C_F$
c_{-1}/a_0	$-3.00000000000000 \times C_F$	$-3 \times C_F$
c_{-2}/a_0	$-2.00000000000000 \times C_F$	$-2 \times C_F$

A.3 $e^+e^- \rightarrow t\bar{t}$

This example has been produced twice: once with the default model file and once with a model file imported from LanHEP [55]. Thus it also can serve as an example of how to import model parameters from LanHEP. The result is given in dimensional reduction, and no renormalisation terms are included.

parameters

M_Z	91.1876	Γ_Z	2.4952
M_W	$\cos \theta_w M_Z$	$\sin \theta_w$	0.47303762
m_t	172.5	μ^2	m_t^2

The following results are obtained with the above parameters and the kinematic point of Table 14.

result $e^+e^- \rightarrow t\bar{t}$

	GoSAM	analytic
a_0	6.3620691850584166	6.3620691850631061
c_0/a_0	13.182472828297422	13.182472828302023
c_{-1}/a_0	12.211527682024421	12.211527682032367
c_{-2}/a_0	0	0

A.4 $u\bar{u} \rightarrow d\bar{d}$

This example has been produced twice: once in the 't Hooft Veltman (HV) scheme and once with dimensional reduction (DRED). Only the result in the HV scheme will be

listed below, for the DRED calculation see the directory `uudd_dred`.

parameters			
μ	91.188	N_f	2

Using the above parameters and the phase space point of Table 15 we obtain the following numbers.

result $u\bar{u} \rightarrow d\bar{d}$		
	GoSAM(HV)	Ref. [103]
a_0	0.28535063700913421	0.28535063700913416
c_0/a_0	-2.7940629929270155	-2.7940629929268876
c_{-1}/a_0	-6.4881359148866604	-6.4881359148866391
c_{-2}/a_0	-5.333333333333333	-5.333333333333333

A.5 $gg \rightarrow gg$

This example has been produced both with the default model file and with a model file imported from LanHEP. Further, it has been calculated in the 't Hooft Veltman scheme and in the dimensional reduction scheme. Only the results in the 't Hooft Veltman scheme are listed below, for further details please see the subdirectories `gggg_dred` and `gggg_lhep`. The result is for the helicity configuration $g(+)g(+) \rightarrow g(-)g(-)$, and pure Yang-Mills theory, i.e. fermion loops are not included.

parameters			
μ^2	442	N_f	0
α_s	0.13		

Evaluating the amplitude for above parameters and the phase space point given in Table 16 we obtain the following results.

result $gg \rightarrow gg$		
	GoSAM(HV)	Ref. [104]
a_0	14.120983050796795	14.120983050796804
c_0/a_0	-124.0247557942351	-124.02475579423495
c_{-1}/a_0	55.003597347101078	55.003597347101035
c_{-2}/a_0	-12.000000000000000	-12

A.6 $gg \rightarrow gZ$

As this process has no tree level amplitude, the result is for the one-loop amplitude squared.

parameters			
μ^2	s_{12}	α_s	1
M_Z	91.1876	Γ_Z	0
$\sin \theta_w$	0.4808222	M_W	$\cos \theta_w M_Z$
N_f	2		

With the above parameters and the kinematics given in Table 17 we obtain the following result.

result $gg \rightarrow gZ$		
	GoSAM	Ref. [105]
a_0	-	-
$ \mathcal{M} _{1\text{-loop}}^2$	0.1075742599502829	0.10757425995048300

A.7 $d\bar{d} \rightarrow t\bar{t}$

This example has been calculated in the 't Hooft Veltman scheme and in the dimensional reduction scheme. Only the

Table 15 Kinematic point used in $u\bar{u} \rightarrow d\bar{d}$

	E	p_x	p_y	p_z
u	102.6289752320661	0	0	102.6289752320661
\bar{u}	102.6289752320661	0	0	-102.6289752320661
d	102.6289752320661	-85.98802977488269	-12.11018104528534	54.70017191625945
\bar{d}	102.6289752320661	85.98802977488269	12.11018104528534	-54.70017191625945

Table 16 Kinematic point used in $gg \rightarrow gg$

	E	p_x	p_y	p_z
p_1	220.9501779577791	0	0	220.9501779577791
p_2	220.9501779577791	0	0	-220.9501779577791
p_3	220.9501779577791	119.9098300357375	183.0492135511419	-30.55485589367430
p_4	220.9501779577791	-119.9098300357375	-183.0492135511419	30.55485589367430

Table 17 Kinematic point used in $gg \rightarrow gZ$

	E	p_x	p_y	p_z
g	100	0	0	100
g	100	0	0	-100
g	79.2120540156	3.65874234516586	-25.1245942606679	75.0327786308013
Z	120.7879459844	-3.65874234516586	25.1245942606679	-75.0327786308013

results in the 't Hooft Veltman scheme are listed below, for the renormalised amplitude with $N_f = 5$ and the top mass renormalised on-shell.

For further details please see the subdirectories ddt and ddt_dred.

parameters

m_t	172.5	μ^2	m_t^2
α_s	1	N_f	5

With the above parameters and the kinematics given in Table 18 we obtain the following results.

result $d\bar{d} \rightarrow t\bar{t}$

	GoSAM(HV)	Ref. [27, 106] (MCFM)
a_0	0.43024349783870747	0.43024349783867882
c_0/a_0	-22.526901042662193	-22.526901042658068
c_{-1}/a_0	10.579577611830414	10.579577611830567
c_{-2}/a_0	-2.6666666666666599	-2.666666666666721

A.8 $gg \rightarrow t\bar{t}$

The result is for the renormalised amplitude in the HV scheme.

Table 18 Kinematic point used in $d\bar{d} \rightarrow t\bar{t}$

	E	p_x	p_y	p_z
d	74.7646520969852	0	0	74.7646520969852
\bar{d}	6067.88254935176	0	0	-6067.88254935176
t	5867.13826404309	16.7946967430656	169.437140279981	-5862.12966020487
\bar{t}	275.508937405653	-16.7946967430656	-169.437140279981	-130.988237049907

Table 19 Kinematic point used in $gg \rightarrow t\bar{t}$

	E	p_x	p_y	p_z
g	137.84795086008967	0.	0.	137.84795086008967
g	3161.1731634194916	0.	0.	-3161.1731634194916
t	3058.6441209877348	16.445287185144903	165.91204201912493	-3049.2945357402382
\bar{t}	240.37699329184659	-16.445287185144903	-165.91204201912493	25.969323180836145

parameters

m_t	171.2	Γ_t	0
N_f	5	μ	71.2

With the above parameters and the kinematics given in Table 19 we obtain the following results.

result $gg \rightarrow t\bar{t}$

	GoSAM(HV)	Ref. [27, 106] (MCFM)
a_0	4.5576116986983433	4.5576116986983424
c_0/a_0	15.352143751168184	15.352143750919995
c_{-1}/a_0	-27.235240992743407	-27.235240936279297
c_{-2}/a_0	-6.0	-6.0

A.9 $bg \rightarrow Hb$

For this process the mass of the b-quark is set to zero. However, in order to have a coupling between the b-quark and the Higgs boson, the following Yukawa coupling is implemented in the model file:

$$\mathcal{L}_{\text{yuk}} = Y_{Hb} \bar{\psi}_L \psi_R \phi, \quad Y_{Hb} = \frac{\bar{m}_b(\mu)}{v}.$$

parameters

m_b	0	$\bar{m}_b(\mu)$	2.937956
m_H	120	v	246.2185
μ	91.188		

With the above parameters and the kinematics given in Table 20 we obtain the following results.

result $bg \rightarrow Hb$

	GoSAM(HV)	Refs. [39, 107]
$a_0 \cdot 10^7$	2.09926265849001642	2.09926265848997195
c_0/a_0	-24.131948141318752	-24.131948141995107
c_{-1}/a_0	11.957924609547224	11.957924605423791
c_{-2}/a_0	-5.66666666666666643	-5.66666666666666670

A.10 $H \rightarrow \gamma\gamma$

The decay width $\Gamma_{H \rightarrow \gamma\gamma}$ of this loop induced process is known analytically at lowest order. For comparison we used the equations including the top loop and the bosonic contribution given in [108, 109]. The decay width can be expressed as

$$\Gamma_{H \rightarrow \gamma\gamma} = \frac{G_F \alpha^2 m_H^3}{128 \sqrt{2} \pi^3} \cdot \hat{\Gamma}(\tau_W, \tau_t), \quad (\text{A.1})$$

where $\tau_i = m_i^2/(4m_H^2)$ for $i = W, t$.

parameters

m_H	124.5	m_t	172.5
m_W	80.398		

Table 20 Kinematic point used in $bg \rightarrow Hb$

	E	p_x	p_y	p_z
b	250	0	0	250
g	250	0	0	-250
H	264.4	-83.84841332241601	-86.85350630148753	-202.3197272300720
b	235.6	83.84841332241601	86.85350630148753	202.3197272300720

Table 21 Kinematic point used in $u\bar{d} \rightarrow e^- \bar{\nu}_e$

	E	p_x	p_y	p_z
u	100	0	0	100
\bar{d}	100	0	0	-100
e^-	100	75.541566535633046	30.240603423558878	-58.128974100026611
$\bar{\nu}_e$	100	-75.541566535633046	-30.240603423558878	58.128974100026611

result $H \rightarrow \gamma\gamma$

	GoSAM	Refs. [108, 109]
$\hat{\Gamma}(\tau_W, \tau_t)$	3.366785118586698	3.36678512043889

A.11 $u\bar{d} \rightarrow e^- \bar{\nu}_e$

This example has been calculated in the 'tHooft Veltman scheme and in the dimensional reduction scheme. Only the results in the 'tHooft Veltman scheme are listed below, for the renormalised amplitude. In addition to a calculation with the default model file, calculations using LanHEP [55] and UFO [54] are also contained in the examples directory.

parameters

\sqrt{s}	200	μ	91.1876
------------	-----	-------	---------

With the above parameters and the kinematics given in Table 21 we obtain the following results.

result $u\bar{d} \rightarrow e^- \bar{\nu}_e$

	GoSAM(HV)	Ref. [39]
a_0	1.4138127601912656	1.4138127601912673
c_0/a_0	5.4861229357937624	5.4861229357937660
c_{-1}/a_0	0.18879169932851950	0.18879169932852413
c_{-2}/a_0	-2.6666666666666667	-2.6666666666666665

A.12 $u\bar{d} \rightarrow e^- \bar{\nu}_e g$

We list the renormalised amplitude in the HV scheme.

parameters			
M_W	80.398	Γ_W	2.1054
$\sin \theta_w$	0.4808222	M_Z	$M_W / \cos \theta_w$
N_f	5	V_{ud}	0.97419
μ^2	s_{12}		

With the above parameters and the kinematics given in Table 22 we obtain the following results.

result $u\bar{d} \rightarrow e^- \bar{\nu}_e g$			
GoSAM(HV)		Ref. [39]	
$a_0 \cdot 10^7$	2.8398509625435832	$a_0 \cdot 10^7$	2.8398509625435922
c_0/a_0	-8.6052919370147745	c_0/a_0	-8.6052919368774248
c_{-1}/a_0	-18.722010655600936	c_{-1}/a_0	-18.722010655557121
c_{-2}/a_0	-5.666666666666666	c_{-2}/a_0	-5.666666666666667

A.13 $g b \rightarrow e^- \bar{\nu}_e t$

We list the renormalised result in the dimensional reduction scheme.

parameters			
M_W	80.4190	Γ_W	2.04760
M_Z	91.1876	Γ_Z	2.49520
m_t	171.2	Γ_t	0
μ	71.2	e	0.30794906326863203

With the above parameters and the kinematics given in Table 23 we obtain the following results.

Table 22 Kinematic point used in $u\bar{d} \rightarrow e^- \bar{\nu}_e g$

	E	p_x	p_y	p_z
u	500	0	0	500
\bar{d}	500	0	0	-500
e^-	483.244841094218	-86.3112218694181	147.629518147233	-451.975082051212
$\bar{\nu}_e$	279.253370247231	6.62401666401929	-5.58083951102529	279.119009435087
g	237.501788658551	79.6872052053988	-142.048678636208	172.856072616124

Table 23 Kinematic point used in $g b \rightarrow e^- \bar{\nu}_e t$

	E	p_x	p_y	p_z
g	1187.7086110647201	0	0	1187.7086110647201
b	2897.148136260289			-2897.148136260289
e^-	2293.0435558834492	629.81047833131981	258.58120146220904	-2189.6399870328105
$\bar{\nu}_e$	509.48956356743611	144.72113807954338	19.883362437475	-488.098411670514
t	1282.3236278741238	-774.53161641086319	-278.46456389968404	968.29887350775562

result $g b \rightarrow e^- \bar{\nu}_e t$		
GoSAM		Ref. [27, 106] (MCFM)
$a_0 \cdot 10^2$	8.52301540675800134	8.52301540708130106
c_0/a_0	-79.879718568538991	-79.879718569273024
c_{-1}/a_0	26.570185488790770	26.570185487963364
c_{-2}/a_0	-4.3333333333333401	-4.3333333331689596

A.14 $\bar{u} d \rightarrow W^+ W^+ \bar{c} s$

Results are given for the unrenormalised amplitude in the dimensional reduction scheme.

parameters			
μ	80	N_f	5

With the above parameters and the kinematics given in Table 24 we obtain the following results.

result $\bar{u} d \rightarrow W^+ W^+ \bar{c} s$		
GoSAM		Ref. [20, v3]
a_0		
c_0/a_0	23.3596455167118	23.35965
c_{-1}/a_0	13.6255429251954	13.62554
c_{-2}/a_0	-5.3333333333333	-5.33333

Table 24 Kinematic point used in $\bar{u}d \rightarrow W^+W^+\bar{c}s$

	E	p_x	p_y	p_z
\bar{u}	500	0	0	500
d	500	0	0	-500
\bar{c}	54.2314070117999	-7.92796656791140	43.6912823611163	-31.1330162081798
s	214.488870161418	-98.5198083786150	188.592247959949	-27.0607980217775
e^+	85.5312248384887	36.1637837682033	-77.0725048002414	-8.22193223977868
ν_e	181.428811610043	-171.863734086635	-5.61185898481311	-57.8599829481937
μ^+	82.8493010774356	-49.8952157196287	5.51413360058664	-65.9095476235891
ν_μ	381.470385300815	292.042940984587	-155.113300136598	190.185277041519

Appendix B: Explicit reduction of R_2 rational terms

In this Appendix we list all integrals which give rise to R_2 terms as we use these expressions in their explicit construction. We use the definition

$$I_N^{n,\alpha;\mu_1,\dots,\mu_r}(S) = \int \frac{\mu^{2\varepsilon} d^n q}{i\pi^{n/2}} \frac{\hat{q}^{\mu_1} \dots \hat{q}^{\mu_r} (\mu^2)^\alpha}{D_1 \dots D_N} \quad (\text{B.1})$$

with

$$D_l = (q + r_l)^2 - m_l^2$$

and

$$S_{ij} = (r_i - r_j)^2 - m_i^2 - m_j^2. \quad (\text{B.2})$$

The integrals up to $\mathcal{O}(\varepsilon)$ are

$$\varepsilon \cdot I_1^{n,0}(S) = -\frac{1}{2} S_{11}, \quad (\text{B.3})$$

$$\varepsilon \cdot I_1^{n,0;\mu_1}(S) = \frac{1}{2} S_{11} \cdot r_1^{\mu_1}, \quad (\text{B.4})$$

$$I_2^{n,1}(S) = -\frac{1}{6} (S_{11} + S_{12} + S_{22}), \quad (\text{B.5})$$

$$\varepsilon \cdot I_2^{n,0}(S) = 1, \quad (\text{B.6})$$

$$\varepsilon \cdot I_2^{n,0;\mu_1}(S) = -\frac{1}{2} (r_1^{\mu_1} + r_2^{\mu_1}), \quad (\text{B.7})$$

$$\begin{aligned} \varepsilon \cdot I_2^{n,0;\mu_1\mu_2}(S) &= \frac{1}{6} (2r_1^{\mu_1} r_1^{\mu_2} + r_1^{\mu_1} r_2^{\mu_2} + r_2^{\mu_1} r_1^{\mu_2} \\ &\quad + 2r_2^{\mu_1} r_2^{\mu_2}) \\ &\quad - \frac{1}{12} \hat{g}^{\mu_1\mu_2} (S_{11} + S_{12} + S_{22}), \end{aligned} \quad (\text{B.8})$$

$$I_3^{n,1}(S) = \frac{1}{2}, \quad (\text{B.9})$$

$$I_3^{n,1;\mu_1}(S) = -\frac{1}{6} (r_1^{\mu_1} + r_2^{\mu_1} + r_3^{\mu_1}), \quad (\text{B.10})$$

$$\varepsilon \cdot I_3^{n,0;\mu_1\mu_2}(S) = \frac{1}{4} \hat{g}^{\mu_1\mu_2}, \quad (\text{B.11})$$

$$\varepsilon \cdot I_3^{n,0;\mu_1\mu_2\mu_3}(S) = -\frac{1}{12} \sum_{l=1}^3 [\hat{g}^{\bullet\bullet} r_l^\bullet]^{\mu_1\mu_2\mu_3}, \quad (\text{B.12})$$

$$I_4^{n,1;\mu_1\mu_2}(S) = \frac{1}{12} \hat{g}^{\mu_1\mu_2}, \quad (\text{B.13})$$

$$I_4^{n,2}(S) = -\frac{1}{6}, \quad (\text{B.14})$$

$$\varepsilon \cdot I_4^{n,0;\mu_1\mu_2\mu_3\mu_4}(S) = \frac{1}{4!} [\hat{g}^{\bullet\bullet} \hat{g}^{\bullet\bullet}]^{\mu_1\mu_2\mu_3\mu_4}. \quad (\text{B.15})$$

References

1. T. Hahn, Comput. Phys. Commun. **140**, 418 (2001). doi:[10.1016/S0010-4655\(01\)00290-9](https://doi.org/10.1016/S0010-4655(01)00290-9)
2. P. Nogueira, J. Comput. Phys. **105**, 279 (1993). doi:[10.1006/jcph.1993.1074](https://doi.org/10.1006/jcph.1993.1074)
3. T. Hahn, M. Perez-Victoria, Comput. Phys. Commun. **118**, 153 (1999). doi:[10.1016/S0010-4655\(98\)00173-8](https://doi.org/10.1016/S0010-4655(98)00173-8)
4. G. Belanger, F. Boudjema, J. Fujimoto, T. Ishikawa, T. Kaneko et al., Phys. Rep. **430**, 117 (2006). doi:[10.1016/j.physrep.2006.02.001](https://doi.org/10.1016/j.physrep.2006.02.001)
5. A. Denner, S. Dittmaier, M. Roth, L. Wieders, Nucl. Phys. B **724**, 247 (2005)
6. C. Berger, Z. Bern, L.J. Dixon, F. Febres Cordero, D. Forde et al., Phys. Rev. D **80**, 074036 (2009). doi:[10.1103/PhysRevD.80.074036](https://doi.org/10.1103/PhysRevD.80.074036)
7. C. Berger, Z. Bern, L.J. Dixon, F. Febres Cordero, D. Forde et al., Phys. Rev. Lett. **102**, 222001 (2009). doi:[10.1103/PhysRevLett.102.222001](https://doi.org/10.1103/PhysRevLett.102.222001)
8. R. Ellis, K. Melnikov, G. Zanderighi, Phys. Rev. D **80**, 094002 (2009). doi:[10.1103/PhysRevD.80.094002](https://doi.org/10.1103/PhysRevD.80.094002)
9. K. Melnikov, G. Zanderighi, Phys. Rev. D **81**, 074025 (2010). doi:[10.1103/PhysRevD.81.074025](https://doi.org/10.1103/PhysRevD.81.074025)
10. C. Berger, Z. Bern, L.J. Dixon, F. Cordero, D. Forde et al., Phys. Rev. D **82**, 074002 (2010). doi:[10.1103/PhysRevD.82.074002](https://doi.org/10.1103/PhysRevD.82.074002)
11. J.M. Campbell, R. Ellis, C. Williams, Phys. Rev. D **81**, 074023 (2010). doi:[10.1103/PhysRevD.81.074023](https://doi.org/10.1103/PhysRevD.81.074023)
12. A. Bredenstein, A. Denner, S. Dittmaier, S. Pozzorini, Phys. Rev. Lett. **103**, 012002 (2009). doi:[10.1103/PhysRevLett.103.012002](https://doi.org/10.1103/PhysRevLett.103.012002)
13. A. Bredenstein, A. Denner, S. Dittmaier, S. Pozzorini, J. High Energy Phys. **1003**, 021 (2010). doi:[10.1007/JHEP03\(2010\)021](https://doi.org/10.1007/JHEP03(2010)021)
14. G. Bevilacqua, M. Czakon, C. Papadopoulos, R. Pittau, M. Worek, J. High Energy Phys. **0909**, 109 (2009). doi:[10.1088/1126-6708/2009/09/109](https://doi.org/10.1088/1126-6708/2009/09/109)

15. G. Bevilacqua, M. Czakon, C. Papadopoulos, M. Worek, Phys. Rev. Lett. **104**, 162002 (2010). doi:[10.1103/PhysRevLett.104.162002](https://doi.org/10.1103/PhysRevLett.104.162002)
16. T. Binoth, N. Greiner, A. Guffanti, J. Reuter, J.P. Guillet et al., Phys. Lett. B **685**, 293 (2010). doi:[10.1016/j.physletb.2010.02.010](https://doi.org/10.1016/j.physletb.2010.02.010)
17. N. Greiner, A. Guffanti, T. Reiter, J. Reuter, Phys. Rev. Lett. **107**, 102002 (2011). doi:[10.1103/PhysRevLett.107.102002](https://doi.org/10.1103/PhysRevLett.107.102002)
18. G. Bevilacqua, M. Czakon, A. van Hameren, C.G. Papadopoulos, M. Worek, J. High Energy Phys. **1102**, 083 (2011). doi:[10.1007/JHEP02\(2011\)083](https://doi.org/10.1007/JHEP02(2011)083)
19. A. Denner, S. Dittmaier, S. Kallweit, S. Pozzorini, Phys. Rev. Lett. **106**, 052001 (2011). doi:[10.1103/PhysRevLett.106.052001](https://doi.org/10.1103/PhysRevLett.106.052001)
20. T. Melia, K. Melnikov, R. Rontsch, G. Zanderighi, J. High Energy Phys. **1012**, 053 (2010). doi:[10.1007/JHEP12\(2010\)053](https://doi.org/10.1007/JHEP12(2010)053)
21. K. Melnikov, M. Schulze, Nucl. Phys. B **840**, 129 (2010). doi:[10.1016/j.nuclphysb.2010.07.003](https://doi.org/10.1016/j.nuclphysb.2010.07.003)
22. F. Campanario, C. Englert, M. Rauch, D. Zeppenfeld, Phys. Lett. B **704**, 515 (2011). doi:[10.1016/j.physletb.2011.09.072](https://doi.org/10.1016/j.physletb.2011.09.072)
23. R. Frederix, S. Frixione, K. Melnikov, G. Zanderighi, J. High Energy Phys. **1011**, 050 (2010). doi:[10.1007/JHEP11\(2010\)050](https://doi.org/10.1007/JHEP11(2010)050)
24. F. Cascioli, P. Maierhofer, S. Pozzorini, Phys. Rev. Lett. **108**, 111601 (2012). doi:[10.1103/PhysRevLett.108.111601](https://doi.org/10.1103/PhysRevLett.108.111601)
25. C. Berger, Z. Bern, L.J. Dixon, F. Cordero, D. Forde et al., Phys. Rev. Lett. **106**, 092001 (2011). doi:[10.1103/PhysRevLett.106.092001](https://doi.org/10.1103/PhysRevLett.106.092001)
26. H. Ita, Z. Bern, L. Dixon, F. Cordero, D. Kosower et al., Phys. Rev. D **85**, 031501 (2012). doi:[10.1103/PhysRevD.85.031501](https://doi.org/10.1103/PhysRevD.85.031501)
27. J.M. Campbell, R. Ellis, Phys. Rev. D **60**, 113006 (1999). doi:[10.1103/PhysRevD.60.113006](https://doi.org/10.1103/PhysRevD.60.113006)
28. J.M. Campbell, R. Ellis, C. Williams, J. High Energy Phys. **1107**, 018 (2011). doi:[10.1007/JHEP07\(2011\)018](https://doi.org/10.1007/JHEP07(2011)018)
29. K. Arnold, M. Bahr, G. Bozzi, F. Campanario, C. Englert et al., Comput. Phys. Commun. **180**, 1661 (2009). doi:[10.1016/j.cpc.2009.03.006](https://doi.org/10.1016/j.cpc.2009.03.006)
30. K. Arnold, J. Bellm, G. Bozzi, M. Brieg, F. Campanario et al. (2011). [arXiv:1107.4038](https://arxiv.org/abs/1107.4038) [hep-ph]
31. S. Frixione, B.R. Webber, J. High Energy Phys. **0206**, 029 (2002)
32. S. Frixione, F. Stoeckli, P. Torrielli, B.R. Webber, C.D. White (2010). [arXiv:1010.0819](https://arxiv.org/abs/1010.0819) [hep-ph]
33. S. Frixione, P. Nason, C. Oleari, J. High Energy Phys. **0711**, 070 (2007). doi:[10.1088/1126-6708/2007/11/070](https://doi.org/10.1088/1126-6708/2007/11/070)
34. S. Alioli, P. Nason, C. Oleari, E. Re, J. High Energy Phys. **1006**, 043 (2010). doi:[10.1007/JHEP06\(2010\)043](https://doi.org/10.1007/JHEP06(2010)043)
35. A. Kardos, C. Papadopoulos, Z. Trocsanyi, Phys. Lett. B **705**, 76 (2011). doi:[10.1016/j.physletb.2011.09.080](https://doi.org/10.1016/j.physletb.2011.09.080)
36. M. Garzelli, A. Kardos, C. Papadopoulos, Z. Trocsanyi, Europhys. Lett. **96**, 11001 (2011). doi:[10.1209/0295-5075/96/11001](https://doi.org/10.1209/0295-5075/96/11001)
37. A. Kardos, C. Papadopoulos, Z. Trocsanyi (2011). [arXiv:1111.0610](https://arxiv.org/abs/1111.0610) [hep-ph]
38. A. van Hameren, C. Papadopoulos, R. Pittau, J. High Energy Phys. **0909**, 106 (2009). doi:[10.1088/1126-6708/2009/09/106](https://doi.org/10.1088/1126-6708/2009/09/106)
39. V. Hirschi, R. Frederix, S. Frixione, M.V. Garzelli, F. Maltoni et al., J. High Energy Phys. **1105**, 044 (2011). doi:[10.1007/JHEP05\(2011\)044](https://doi.org/10.1007/JHEP05(2011)044)
40. P. Mastrolia, G. Ossola, T. Reiter, F. Tramontano, J. High Energy Phys. **1008**, 080 (2010). doi:[10.1007/JHEP08\(2010\)080](https://doi.org/10.1007/JHEP08(2010)080)
41. G. Cullen, N. Greiner, A. Guffanti, J.P. Guillet, G. Heinrich et al., Nucl. Phys. Proc. Suppl. **205–206**, 67 (2010). doi:[10.1016/j.nuclphysbps.2010.08.021](https://doi.org/10.1016/j.nuclphysbps.2010.08.021)
42. G. Bevilacqua, M. Czakon, M. Garzelli, A. van Hameren, A. Kardos et al. (2011). [arXiv:1110.1499](https://arxiv.org/abs/1110.1499) [hep-ph]
43. L. Reina, T. Schutzmeier (2011). [arXiv:1110.4438](https://arxiv.org/abs/1110.4438) [hep-ph]
44. R. Ellis, Z. Kunszt, K. Melnikov, G. Zanderighi (2011). [arXiv:1105.4319](https://arxiv.org/abs/1105.4319) [hep-ph]
45. G. Ossola, C.G. Papadopoulos, R. Pittau, Nucl. Phys. B **763**, 147 (2007). doi:[10.1016/j.nuclphysb.2006.11.012](https://doi.org/10.1016/j.nuclphysb.2006.11.012)
46. G. Ossola, C.G. Papadopoulos, R. Pittau, J. High Energy Phys. **07**, 085 (2007). doi:[10.1088/1126-6708/2007/07/085](https://doi.org/10.1088/1126-6708/2007/07/085)
47. R. Ellis, W.T. Giele, Z. Kunszt, K. Melnikov, Nucl. Phys. B **822**, 270 (2009). doi:[10.1016/j.nuclphysb.2009.07.023](https://doi.org/10.1016/j.nuclphysb.2009.07.023)
48. J. Vermaseren (2000). [arXiv:math-ph/0010025](https://arxiv.org/abs/math-ph/0010025)
49. G. Cullen, M. Koch-Janusz, T. Reiter, Comput. Phys. Commun. **182**, 2368 (2011). doi:[10.1016/j.cpc.2011.06.007](https://doi.org/10.1016/j.cpc.2011.06.007)
50. T. Reiter, Comput. Phys. Commun. **181**, 1301 (2010). doi:[10.1016/j.cpc.2010.01.012](https://doi.org/10.1016/j.cpc.2010.01.012)
51. T. Binoth, J.P. Guillet, G. Heinrich, E. Pilon, T. Reiter, Comput. Phys. Commun. **180**, 2317 (2009). doi:[10.1016/j.cpc.2009.06.024](https://doi.org/10.1016/j.cpc.2009.06.024)
52. G. Cullen, J. Guillet, G. Heinrich, T. Kleinschmidt, E. Pilon et al., Comput. Phys. Commun. **182**, 2276 (2011). doi:[10.1016/j.cpc.2011.05.015](https://doi.org/10.1016/j.cpc.2011.05.015)
53. G. Heinrich, G. Ossola, T. Reiter, F. Tramontano, J. High Energy Phys. **1010**, 105 (2010). doi:[10.1007/JHEP10\(2010\)105](https://doi.org/10.1007/JHEP10(2010)105)
54. C. Degrande, C. Duhr, B. Fuks, D. Grellscheid, O. Mattelaer et al., Comput. Phys. Commun. **183**, 1201 (2012). doi:[10.1016/j.cpc.2012.01.022](https://doi.org/10.1016/j.cpc.2012.01.022)
55. A. Semenov (2010). [arXiv:1005.1909](https://arxiv.org/abs/1005.1909) [hep-ph]
56. T. Binoth, F. Boudjema, G. Dissertori, A. Lazopoulos, A. Denner et al., Comput. Phys. Commun. **181**, 1612 (2010). doi:[10.1016/j.cpc.2010.05.016](https://doi.org/10.1016/j.cpc.2010.05.016). Dedicated to the memory of, and in tribute to, Thomas Binoth, who led the effort to develop this proposal for Les Houches 2009
57. G. Ossola, C.G. Papadopoulos, R. Pittau, J. High Energy Phys. **0803**, 042 (2008). doi:[10.1088/1126-6708/2008/03/042](https://doi.org/10.1088/1126-6708/2008/03/042)
58. J. Fleischer, T. Riemann, Phys. Rev. D **83**, 073004 (2011). doi:[10.1103/PhysRevD.83.073004](https://doi.org/10.1103/PhysRevD.83.073004)
59. G. van Oldenborgh, J. Vermaseren, Z. Phys. C **46**, 425 (1990). doi:[10.1007/BF01621031](https://doi.org/10.1007/BF01621031)
60. T. Ohl, Comput. Phys. Commun. **90**, 340 (1995). doi:[10.1016/0010-4655\(95\)90137-S](https://doi.org/10.1016/0010-4655(95)90137-S)
61. J. Vermaseren, Comput. Phys. Commun. **83**, 45 (1994). doi:[10.1016/0010-4655\(94\)90034-5](https://doi.org/10.1016/0010-4655(94)90034-5). Axodraw can be obtained from anonymous ftp from ftp.nikhef.nl. It is located in directory pub/form/axodraw. The author's email address is: t68@nikhef.nl
62. T. Reiter, Ph.D. thesis, 2009
63. P. Nason, J. High Energy Phys. **0411**, 040 (2004). doi:[10.1088/1126-6708/2004/11/040](https://doi.org/10.1088/1126-6708/2004/11/040)
64. Z. Xu, D.H. Zhang, L. Chang, Nucl. Phys. B **291**, 392 (1987). doi:[10.1016/0550-3213\(87\)90479-2](https://doi.org/10.1016/0550-3213(87)90479-2)
65. W. Kilian, T. Ohl, J. Reuter, Eur. Phys. J. C **71**, 1742 (2011). doi:[10.1140/epjc/s10052-011-1742-y](https://doi.org/10.1140/epjc/s10052-011-1742-y)
66. G. Ossola, C.G. Papadopoulos, R. Pittau, J. High Energy Phys. **0805**, 004 (2008). doi:[10.1088/1126-6708/2008/05/004](https://doi.org/10.1088/1126-6708/2008/05/004)
67. P. Draggiotis, M. Garzelli, C. Papadopoulos, R. Pittau, J. High Energy Phys. **0904**, 072 (2009). doi:[10.1088/1126-6708/2009/04/072](https://doi.org/10.1088/1126-6708/2009/04/072)
68. M. Garzelli, I. Malamos, R. Pittau, J. High Energy Phys. **1001**, 040 (2010). doi:[10.1007/JHEP01\(2010\)040](https://doi.org/10.1007/JHEP01(2010)040)
69. M. Garzelli, I. Malamos, R. Pittau, J. High Energy Phys. **1101**, 029 (2011). doi:[10.1007/JHEP01\(2011\)029](https://doi.org/10.1007/JHEP01(2011)029)
70. M. Garzelli, I. Malamos, Eur. Phys. J. C **71**, 1605 (2011). doi:[10.1140/epjc/s10052-011-1605-6](https://doi.org/10.1140/epjc/s10052-011-1605-6)
71. P. Nason, S. Dawson, R.K. Ellis, Nucl. Phys. B **303**, 607 (1988). doi:[10.1016/0550-3213\(88\)90422-1](https://doi.org/10.1016/0550-3213(88)90422-1)
72. B. Harris, E. Laenen, L. Phaf, Z. Sullivan, S. Weinzierl, Phys. Rev. D **66**, 054024 (2002). doi:[10.1103/PhysRevD.66.054024](https://doi.org/10.1103/PhysRevD.66.054024)
73. S. Weinzierl (1999). [arXiv:hep-ph/9903380](https://arxiv.org/abs/hep-ph/9903380)
74. A. van Hameren, Comput. Phys. Commun. **182**, 2427 (2011). doi:[10.1016/j.cpc.2011.06.011](https://doi.org/10.1016/j.cpc.2011.06.011)
75. R.K. Ellis, G. Zanderighi, J. High Energy Phys. **02**, 002 (2008). doi:[10.1088/1126-6708/2008/02/002](https://doi.org/10.1088/1126-6708/2008/02/002)

76. G. Yost et al., Phys. Lett. B **204**, 1 (1988). doi:[10.1016/0370-2693\(88\)90505-9](https://doi.org/10.1016/0370-2693(88)90505-9)
77. C. Caso et al., Eur. Phys. J. C **3**, 1 (1998). doi:[10.1007/s10052-998-0104-x](https://doi.org/10.1007/s10052-998-0104-x)
78. S. Catani, M. Seymour, Nucl. Phys. B **485**, 291 (1997). doi:[10.1016/S0550-3213\(96\)00589-5](https://doi.org/10.1016/S0550-3213(96)00589-5)
79. S. Catani, S. Dittmaier, Z. Trocsanyi, Phys. Lett. B **500**, 149 (2001). doi:[10.1016/S0370-2693\(01\)00065-X](https://doi.org/10.1016/S0370-2693(01)00065-X)
80. N.D. Christensen, C. Duhr, Comput. Phys. Commun. **180**, 1614 (2009). doi:[10.1016/j.cpc.2009.02.018](https://doi.org/10.1016/j.cpc.2009.02.018)
81. T. Gleisberg, S. Hoeche, F. Krauss, M. Schonherr, S. Schumann et al., J. High Energy Phys. **0902**, 007 (2009). doi:[10.1088/1126-6708/2009/02/007](https://doi.org/10.1088/1126-6708/2009/02/007)
82. F. Krauss, R. Kuhn, G. Soff, J. High Energy Phys. **0202**, 044 (2002).
83. T. Gleisberg, F. Krauss, Eur. Phys. J. C **53**, 501 (2008). doi:[10.1140/epjc/s10052-007-0495-0](https://doi.org/10.1140/epjc/s10052-007-0495-0)
84. M. Schonherr, F. Krauss, J. High Energy Phys. **0812**, 018 (2008). doi:[10.1088/1126-6708/2008/12/018](https://doi.org/10.1088/1126-6708/2008/12/018)
85. S. Hoeche, F. Krauss, M. Schonherr, F. Siegert, J. High Energy Phys. **1104**, 024 (2011). doi:[10.1007/JHEP04\(2011\)024](https://doi.org/10.1007/JHEP04(2011)024)
86. S. Hoeche, F. Krauss, M. Schonherr, F. Siegert (2011)
87. <http://projects.hepforge.org/sherpa/>, 2011
88. J.H. Kuhn, A. Kulesza, S. Pozzorini, M. Schulze, Nucl. Phys. B **797**, 27 (2008). doi:[10.1016/j.nuclphysb.2007.12.029](https://doi.org/10.1016/j.nuclphysb.2007.12.029)
89. T. Gehrmann, N. Greiner, J. High Energy Phys. **12**, 050 (2010). doi:[10.1007/JHEP12\(2010\)050](https://doi.org/10.1007/JHEP12(2010)050)
90. G. Gounaris, P. Porfyriadis, F. Renard, Eur. Phys. J. C **9**, 673 (1999). doi:[10.1007/s100529900079](https://doi.org/10.1007/s100529900079)
91. W. Beenakker et al., Phys. Rev. Lett. **83**, 3780 (1999). doi:[10.1103/PhysRevLett.83.3780](https://doi.org/10.1103/PhysRevLett.83.3780)
92. R. Frederix, T. Gehrmann, N. Greiner, J. High Energy Phys. **0809**, 122 (2008). doi:[10.1088/1126-6708/2008/09/122](https://doi.org/10.1088/1126-6708/2008/09/122)
93. R. Frederix, T. Gehrmann, N. Greiner, J. High Energy Phys. **1006**, 086 (2010). doi:[10.1007/JHEP06\(2010\)086](https://doi.org/10.1007/JHEP06(2010)086)
94. J. Alwall, P. Demin, S. de Visscher, R. Frederix, M. Herquet et al., J. High Energy Phys. **0709**, 028 (2007). doi:[10.1088/1126-6708/2007/09/028](https://doi.org/10.1088/1126-6708/2007/09/028)
95. A.D. Martin, W.J. Stirling, R.S. Thorne, G. Watt, Eur. Phys. J. C **63**, 189 (2009). doi:[10.1140/epjc/s10052-009-1072-5](https://doi.org/10.1140/epjc/s10052-009-1072-5)
96. B. Feigl, H. Rzehak, D. Zeppenfeld (2011)
97. S. Actis, P. Mastrolia, G. Ossola, Phys. Lett. B **682**, 419 (2010). doi:[10.1016/j.physletb.2009.11.035](https://doi.org/10.1016/j.physletb.2009.11.035)
98. N. Greiner, A. Guffanti, J.P. Guillet, T. Reiter, J. Reuter, PoS **DIS2010**, 156 (2010)
99. T. Binoth, G. Cullen, N. Greiner, A. Guffanti, J.P. Guillet et al., PoS **RADCOR2009**, 026 (2010)
100. F. Febres Cordero, L. Reina, D. Wackeroth, Phys. Rev. D **74**, 034007 (2006). doi:[10.1103/PhysRevD.74.034007](https://doi.org/10.1103/PhysRevD.74.034007)
101. S. Badger, J.M. Campbell, R. Ellis, J. High Energy Phys. **1103**, 027 (2011). doi:[10.1007/JHEP03\(2011\)027](https://doi.org/10.1007/JHEP03(2011)027)
102. R. Kleiss, W. Stirling, S. Ellis, Comput. Phys. Commun. **40**, 359 (1986). doi:[10.1016/0010-4655\(86\)90119-0](https://doi.org/10.1016/0010-4655(86)90119-0)
103. R. Ellis, J. Sexton, Nucl. Phys. B **269**, 445 (1986). doi:[10.1016/0550-3213\(86\)90232-4](https://doi.org/10.1016/0550-3213(86)90232-4)
104. T. Binoth, J. Guillet, G. Heinrich, J. High Energy Phys. **0702**, 013 (2007). doi:[10.1088/1126-6708/2007/02/013](https://doi.org/10.1088/1126-6708/2007/02/013)
105. J. van der Bij, E. Glover, Nucl. Phys. B **313**, 237 (1989). doi:[10.1016/0550-3213\(89\)90317-9](https://doi.org/10.1016/0550-3213(89)90317-9)
106. J.M. Campbell, R.K. Ellis, Phys. Rev. D **62**, 114012 (2000). doi:[10.1103/PhysRevD.62.114012](https://doi.org/10.1103/PhysRevD.62.114012)
107. J.M. Campbell, R. Ellis, F. Maltoni, S. Willenbrock, Phys. Rev. D **67**, 095002 (2003). doi:[10.1103/PhysRevD.67.095002](https://doi.org/10.1103/PhysRevD.67.095002)
108. U. Aglietti, R. Bonciani, G. Degrandi, A. Vicini, Phys. Lett. B **595**, 432 (2004). doi:[10.1016/j.physletb.2004.06.063](https://doi.org/10.1016/j.physletb.2004.06.063)
109. R. Harlander, P. Kant, J. High Energy Phys. **0512**, 015 (2005). doi:[10.1088/1126-6708/2005/12/015](https://doi.org/10.1088/1126-6708/2005/12/015)